

Calorimetry at a Future Linear Collider

Steven Green
of Emmanuel College

A dissertation submitted to the University of Cambridge
for the degree of Doctor of Philosophy

Abstract

This thesis describes the optimisation of the calorimeter design for collider experiments at the future Compact LInear Collider (CLIC) and the International Linear Collider (ILC). The detector design of these experiments is built around high-granularity Particle Flow Calorimetry that, in contrast to traditional calorimetry, uses the energy measurements for charged particles from the tracking detectors. This can only be realised if calorimetric energy deposits from charged particles can be separated from those of neutral particles. This is made possible with fine granularity calorimeters and sophisticated pattern recognition software, which is provided by the PandoraPFA algorithm. This thesis presents results on Particle Flow calorimetry performance for a number of detector configurations. To obtain these results a new calibration procedure was developed and applied to the detector simulation and reconstruction to ensure optimal performance was achieved for each detector configuration considered.

This thesis also describes the development of a software compensation technique that vastly improves the intrinsic energy resolution of a Particle Flow Calorimetry detector. This technique is implemented within the PandoraPFA framework and demonstrates the gains that can be made by fully exploiting the information provided by the fine granularity calorimeters envisaged at a future linear collider.

A study of the sensitivity of the CLIC experiment to anomalous gauge couplings that effect vector boson scattering processes is presented. These anomalous couplings provide insight into possible beyond standard model physics. This study, which utilises the excellent jet energy resolution from Particle Flow Calorimetry, was performed at centre-of-mass energies of 1.4 TeV and 3 TeV with integrated luminosities of 1.5ab^{-1}

and $2ab^{-1}$ respectively. The precision achievable at CLIC is shown to be approximately one to two orders of magnitude better than that currently offered by the LHC.

In addition, a study into various technology options for the CLIC vertex detector is described.

Declaration

This dissertation is the result of my own work, except where explicit reference is made to the work of others, and has not been submitted for another qualification to this or any other university. This dissertation does not exceed the word limit for the respective Degree Committee.

Steven Green

Acknowledgements

Of the many people who deserve thanks, some are particularly prominent, such as my supervisor . . .

Contents

| | | |
|----------|--|-----------|
| 1 | Introduction | 1 |
| 1.1 | Future Linear Colliders | 3 |
| 1.1.1 | The International Linear Collider | 3 |
| 1.1.2 | The Compact Linear Collider | 4 |
| 1.1.2.1 | Experimental Conditions at CLIC | 4 |
| 1.1.2.2 | Beam-Related Backgrounds at CLIC | 6 |
| 2 | Anomalous Gauge Coupling Theory | 9 |
| 2.1 | The Standard Model | 9 |
| 2.2 | Higgs Physics | 13 |
| 2.2.1 | Spontaneous Symmetry Breaking | 13 |
| 2.2.2 | Electroweak Interactions | 14 |
| 2.2.2.1 | Custodial Symmetry | 16 |
| 2.3 | Effective Field Theory | 18 |
| 2.4 | Electroweak Chiral Lagrangian | 19 |
| 3 | Particle Flow Calorimetry for Future Linear Colliders | 23 |
| 3.1 | Particle Flow Calorimetry | 23 |
| 3.2 | International Large Detector | 26 |
| 3.2.1 | Overview | 26 |
| 3.2.2 | Vertex Detector | 27 |
| 3.2.3 | Time Projection Chamber | 28 |
| 3.2.4 | Supplemental Silicon Tracking System | 29 |
| 3.2.5 | Electromagnetic Calorimeter | 32 |
| 3.2.6 | Hadronic Calorimeter | 33 |
| 3.2.7 | Solenoid, Yoke and Muon System | 35 |
| 3.2.8 | Forward Calorimetry | 36 |
| 3.3 | Simulation | 38 |
| 3.4 | CLIC ILD | 39 |

| | | |
|----------|--|-----------|
| 3.5 | Particle Flow Reconstruction | 40 |
| 3.5.1 | PandoraPFA | 41 |
| 3.6 | Performance | 45 |
| 3.6.1 | Jet Energy Resolution | 45 |
| 3.6.2 | Decomposition of the Jet Energy Resolution | 47 |
| 3.6.3 | Single Particle Energy Resolution | 48 |
| 3.7 | Summary of ILD Detector Performance | 49 |
| 4 | Capacitively Coupled Pixel Detectors for the CLIC Vertex Detector | 55 |
| 4.1 | Introduction | 55 |
| 4.1.1 | HV-CMOS | 56 |
| 4.1.2 | CLIC ASICs | 58 |
| 4.1.2.1 | CLICpix | 59 |
| 4.1.3 | Capacitive Coupling | 60 |
| 4.2 | Device Fabrication | 60 |
| 4.3 | Device Characterisation | 61 |
| 4.3.1 | Source Measurements | 62 |
| 4.3.1.1 | Experimental Setup | 62 |
| 4.3.1.2 | Analysis | 63 |
| 4.3.1.3 | Results: Rise Time vs Pulse Height | 64 |
| 4.3.1.4 | Results: ToT vs Pulse Height | 66 |
| 4.3.1.5 | Results: Cross Couplings | 67 |
| 4.3.2 | Test Pulse Calibration | 69 |
| 4.3.2.1 | Experimental Setup | 69 |
| 4.3.2.2 | Analysis | 69 |
| 4.3.2.3 | Results | 70 |
| 4.4 | Test Beam Analysis | 73 |
| 4.4.1 | Test Beam Setup | 75 |
| 4.4.2 | Analysis | 75 |
| 4.4.3 | Results | 76 |
| 4.5 | Conclusions | 77 |
| | Bibliography | 81 |

*“Writing in English is the most ingenious torture
ever devised for sins committed in previous lives.”*

— James Joyce

Chapter 1

Introduction

“There, sir! that is the perfection of vessels!”

— Jules Verne, 1828–1905

The Standard Model has proven to be one of the greatest accomplishments of modern day particle physics. It has have been used to make countless predictions of various physics processes across a wide range of energies that have proven to be consistent with experimental measurements. The final piece of the Standard Model to be discovered was the Higgs boson, which was found by the ATLAS [1] and CMS [2] experiments at the Large Hadron Collider (LHC) in 2012.

Despite the remarkable descriptive power of the Standard Model, there are a number of features in the universe that it does not provide a description for. How does gravity fit into the Standard Model? Why is there an excess of matter over antimatter in the observable universe? What is "dark matter" and "dark energy"? How does "dark matter" couple with the particles in the Standard Model? What are the properties of the Higgs field in the Standard Model? While the LHC and previous generations of particle collider experiment have had enormous success in validating the Standard Model and searching for new physics, it is clear that there is more work to be done.

The linear collider experiments are proposals for the next generation of particle collider experiment. These experiments are TeV scale e^+e^- colliders with an emphasis on precision measurements. The physics programme for the linear collider is designed to complement and extend the work done at the LHC and to develop our understanding of particle physics. One of the primary goals of the linear collider experiments is to

study the Higgs field of the Standard Model. A detailed description of the Higgs field could help in the description of "dark matter" as many extensions of the Standard Model Higgs field contain particles that fit the properties of "dark matter". The linear collider experiments will also provide a detailed description of the properties of the top quark. This will complement the Higgs study because the strongest couplings for the Higgs in the Standard Model occurs with the top quark. Another goal of the linear collider experiments is to provide high precision measurements of the electroweak sector in the Standard Model. As the electroweak sector is the only place in the Standard Model where CP violation can occur, a detailed description will help to determine why there is an excess of matter over antimatter in the universe. Furthermore, the linear collider will expand the descriptive reach for many Standard Model extensions such as supersymmetry (SUSY).

The linear collider experiments place emphasis on precision measurements. As well as searching for beyond Standard Model physics, precision measurements will guide the future direction of experimental particle physics. Precision measurements have helped to guide the course of particle physics experiments in the past; LEP electroweak data, which gave indirect information about the lightness of the Higgs boson, was used to build the physics case for the LHC. By colliding electrons and positrons, which are fundamental particles, the experimental conditions found at the linear collider will be far cleaner than those at the LHC, which makes it easier to perform precision measurements. High precision measurements are made possible at the linear collider due to the use of particle flow calorimetry, which is a revolutionary technique in calorimetry that offers exceptional energy resolution for jets. This paradigm shift means the linear collider detectors are significantly different from those found in previous generations of particle colliders. As the detector design is continually evolving, the ongoing research in this area is vital for determining the overall success of these proposed experiments.

This thesis is organised as follows. Chapter 2 contains a summary of the Standard Model as well as an outline of the physics of interest related to the analysis presented in chapter ???. Chapter 4 presents a study into a novel technology option for the Compact LInear Collider (CLIC) vertex detector. Chapter ?? contains numerous studies related to the treatment of energy deposits in the linear collider simulation. This begins with an outline of the calibration procedure for the linear collider detector simulation. This is followed by a number of novel software techniques aimed at improving the energy resolution of a calorimeter designed for particle flow calorimetry. Finally, the chapter concludes with a study of the timing requirements applied in the software trigger that will

be used at the linear collider experiment. Chapter ?? presents an optimisation study of the linear collider calorimeters. The starker contrast in detector design, when comparing particle flow calorimetry to tradition calorimetry, is the design of the calorimeters. As the linear collider experiments will be the first experiments purposefully built with particle flow calorimetry in mind, this study will be vital for guiding detector construction. Chapter ?? contains a study into anomalous gauge couplings that are sensitive to massive gauge boson quartic vertices at the CLIC experiment. This study is of particular interest as it provides a detailed probe of the electroweak symmetry breaking sector of the Standard Model as well as showing CLICs sensitivity to a possible extension to the Standard Model. The thesis concludes with a summary in chapter ??.

1.1 Future Linear Colliders

There are two proposed future linear colliders; the International Linear Collider (ILC) and the Compact LInear Collider (CLIC). These colliders are both e^+e^- colliders with focus upon precision measurements, however, they operate at different collision energies, which presents each experiment with its own unique challenges. One benefit of a linear collider is that it is possible to stage the experiment at several different energies throughout the experiments lifetime

1.1.1 The International Linear Collider

The ILC, shown in figure 1.1, initially plans to operate at a centre-of-mass energy of 250 GeV to study the Higgs boson in detail through the Higgstrahlung process ($e^+e^- \rightarrow ZH$) [3]. This analysis of this process makes it possible to examine all the decays of the Higgs boson with high precision. The next phase of operation will increase the collision energy to 500 GeV. This will extend the study of the Higgs, making it possible to observe the Higgs coupling with the top quark and to determine self interactions of the Higgs. Furthermore, at this energy, it will be possible to search for evidence for SUSY and extended Higgs states. Finally, there is an option to increase the centre-of-mass up to 1 TeV, which would extend the search for SUSY and composite Higgs models.

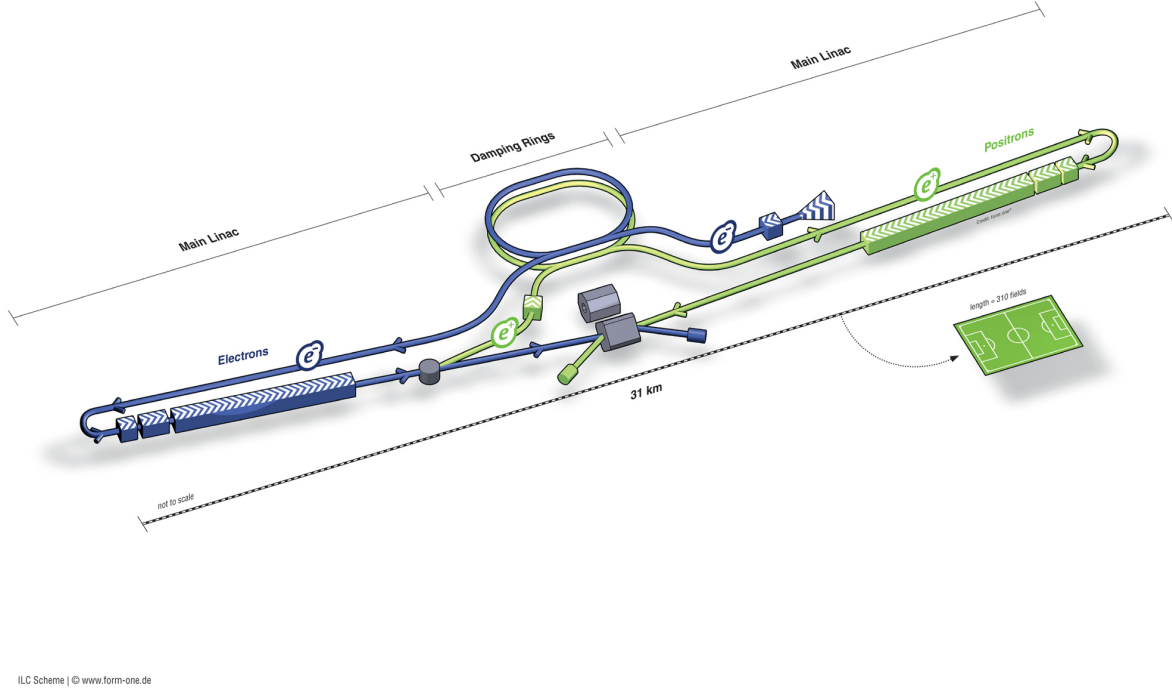


Figure 1.1: Schematic layout of the ILC, indicating all the major subsystems (not to scale). Figure taken from [3].

1.1.2 The Compact Linear Collider

The CLIC experiment, shown in figure 1.2, plans to operate with maximum collision energy of 3 TeV [4]. CLIC will also operate at intermediate energy stages, however, these energies are to be determined by the ongoing work at the LHC. The large collision energy of CLIC gives it a greater physics reach for searching for extensions to the Standard Model, e.g. SUSY, that would be inaccessible at ILC-like energies. Although the exact energies for the staging of the CLIC experiment are not certain, CLIC will operate at a low collision energy during staging, 380 GeV, to study the Higgs. The higher energy stages of the CLIC experiment will provide access to different channels for studying Higgs couplings, as shown by figure 1.3.

1.1.2.1 Experimental Conditions at CLIC

The CLIC experiment will operate in a unique environment in comparison to either the ILC or previous generations of lepton colliders. It is vital that this is properly accounted for when determining the physics potential that CLIC has to offer. The following aspects of the CLIC experiment present the largest challenges to the physics potential:

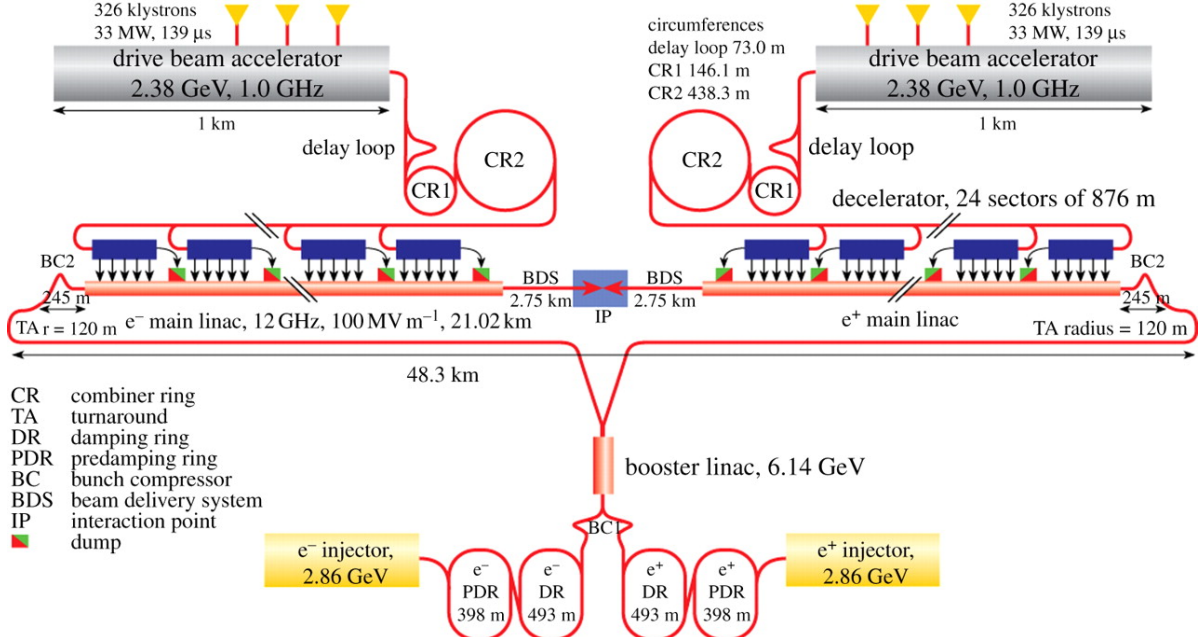


Figure 1.2: CLIC layout at 3 TeV. Figure taken from [5].

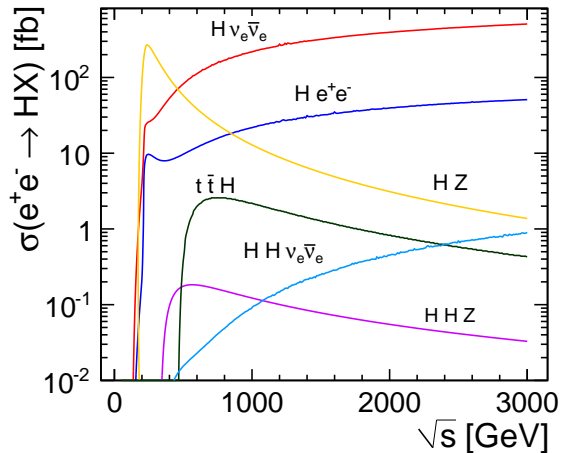


Figure 1.3: Cross section for production mechanisms of the Standard Model Higgs boson as a function of the collision energy. The cross sections were calculated assuming a Higgs mass of 120 GeV. Figure taken from [4].

- The high bunch charge density. The small beam size at the impact point produces very large electromagnetic fields. These fields can interact with the opposite beam particles causing them to radiate photons in an effect known as beamstrahlung. Beamstrahlung acts to reduce the collision energy of the e^+e^- pairs.

- Beam related backgrounds. Beamstrahlung photons can subsequently interact to produce background events that must be accounted for. Dominant backgrounds of this form that cannot be easily vetoed in the reconstruction include incoherent pair production of e^+e^- and $\gamma\gamma \rightarrow hadrons$. While these backgrounds are also problematic for the ILC experiment, the lower collision energy means it has a much smaller impact on performance.
- Fast readout technology. The CLIC bunch train consists of 312 bunches with a repetition rate of 50 Hz. Each bunch is separated by 0.5 ns, therefore, it will be necessary to integrate over multiple bunch crossing when reading out the detectors. This places tight constraints on all detector electrical readout speeds and time resolutions.

1.1.2.2 Beam-Related Backgrounds at CLIC

The primary sources of background for the CLIC experiment are as follows:

- e^+e^- pair creation from the interaction of a beamstrahlung photons with the opposing beam. The different mechanisms for pair creation are as follows:
 - **Coherent pair production.** This mechanism involves the interaction of a real beamstrahlung photon with the electromagnetic field from the opposing beam.
 - **Trident pair production.** This mechanism involves the interaction of a virtual beamstrahlung photon with the electromagnetic field from the opposing beam.
 - **Incoherent pair production.** This mechanism involves the interaction of a real or virtual beamstrahlung photon with the individual particles in the opposing beam.
- $\gamma\gamma \rightarrow hadrons$ events from the interaction of real or virtual beamstrahlung photons with each other.
- Beam halo muons that arise from interactions of the beam particles during collimation. The dominant mechanisms producing beam halo muons are photon conversions into muon pairs ($\gamma e^- \rightarrow \mu^+ \mu^- e^-$) and annihilation of positrons with atomic e^- into muon pairs ($e^+e^- \rightarrow \mu^+ \mu^-$) [6].

These backgrounds must be properly addressed to get a true measure of the physics potential CLIC has to offer. Coherent and trident pair production are not dominant sources of background because they have low transverse momenta and are collinear with the outgoing beam, as figure 1.4 shows. This is not the case for incoherent pair production of e^+e^- , which is dominant in the forward regions of the detector, and $\gamma\gamma \rightarrow \text{hadrons}$, which is dominant in the tracker and the calorimeters (with the exception of low radii in the calorimeter endcaps) [4, 7]. Beam halo muons are not a major source of background either as they can be easily removed during the reconstruction because they produce a clear signal in the detector. An algorithm was developed within the PandoraPFA framework for this purpose and it was found to be highly effective at removing the beam halo muon backgrounds [4].

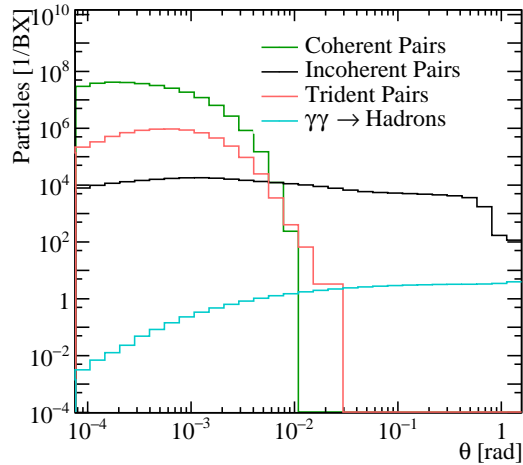


Figure 1.4: Angular distribution of number of particles for beam induced backgrounds for CLIC at $\sqrt{s} = 3$ TeV. Figure taken from [4].

The dominant beam-related background found at the CLIC experiment is $\gamma\gamma \rightarrow \text{hadrons}$. Table 1.1 shows that $\gamma\gamma \rightarrow \text{hadrons}$ backgrounds deposit more energy within the detector than the incoherent pair production. Each bunch crossing at $\sqrt{s} = 3$ TeV CLIC contains an average of 3.2 $\gamma\gamma \rightarrow \text{hadrons}$ events and 3×10^5 incoherent pairs, however, the vast majority of incoherent pairs are produced with low transverse momenta and are collinear with the outgoing beam.

| Subdetector | Incoherent Pairs [TeV] | $\gamma\gamma \rightarrow hadrons$ [TeV] |
|-------------------|------------------------|--|
| ECal Endcaps | 2 | 11 |
| ECal Barrel | - | 1.5 |
| HCal Endcaps | 16 | 6 |
| HCal Barrel | 0 | 0.3 |
| Total Calorimeter | 18 | 19 |
| Central Tracker | - | 7 |

Table 1.1: Summary of the background conditions at $\sqrt{s} = 3$ TeV for the CLIC_ILD detector model. The numbers correspond to the background for an entire CLIC bunch train. The reconstructed calorimeter energies are integrated over 300 ns from the start of the bunch train. The backgrounds in the HCal from incoherent pairs are pessimistic as no attempts to mitigate the effect of neutrons from incoherent pair interactions in the BeamCal have been made. Figure taken from [4].

Chapter 2

Anomalous Gauge Coupling Theory

*“"Meaningless! Meaningless!" says the Teacher. "Utterly meaningless!
Everything is meaningless."”*

— Ecclesiastes 1:2

Presented in chapter ?? is an analysis of the sensitivity of the CLIC experiment to the anomalous gauge couplings α_4 and α_5 through the vector boson scattering process. Here a brief description of the Standard Model of particle physics and a deeper discussion of the anomalous coupling theory studied in chapter ?? is given.

2.1 The Standard Model

The Standard Model is a non-abelian gauge theory of the $SU(3) \times SU(2)_L \times U(1)$ symmetry group. It provides a description of three of the four fundamental forces of nature: the electromagnetic, weak and strong nuclear forces [8, 9]. The Standard Model contains a total of 24 fermion fields: six flavours of quark, each with three colours, and six leptons. A summary of the properties of these particles is given in table 2.1 and 2.2. As these fields, ψ , are spin- $\frac{1}{2}$, they obey the Dirac equation

$$\mathcal{L} = \bar{\psi}(i\cancel{\partial} - m)\psi , \quad (2.1)$$

where \mathcal{L} is the Lagrangian density and m is a mass term. The derivative term, $\cancel{\partial} = \gamma^\mu \partial_\mu$, represents a summation over the partial derivate, $\partial^\mu = (\frac{\partial}{\partial t}, \frac{\partial}{\partial x}, \frac{\partial}{\partial y}, \frac{\partial}{\partial z})$, of the field ψ and the gamma matrices, γ^μ . Each of the gauge transformations of the Standard Model are

defined by a unitary operator U , which acts to transform the vector space, Ψ , formed from a combination of fermion fields, ψ , in the following way

$$\Psi \rightarrow \Psi' = U\Psi . \quad (2.2)$$

In the Standard Mode, the Lagrangian density describing the fermion fields is invariant

| Generation | Particle | Mass [MeV] | Spin | Q/e |
|------------|------------|---------------------------------|-------|-------|
| 1 | e^- | $548.579909070 \pm 0.000000016$ | $1/2$ | -1 |
| | ν_e | | - | $1/2$ |
| 2 | μ^- | $105.6583745 \pm 0.0000024$ | $1/2$ | -1 |
| | ν_μ | | - | $1/2$ |
| 3 | τ^- | 1776.86 ± 0.12 | $1/2$ | -1 |
| | ν_τ | | - | $1/2$ |

Table 2.1: The mass, spin and electric charge (Q) of the leptons found in the Standard Model [10]. Neutrino masses have not been included in the above table as precise measurements are yet to be made. However, oscillations between different neutrino flavour states have been observed, which indicates that the flavour and mass eigenstates differ and that the neutrinos have a non-zero mass. The current upper bound on neutrino mass measurements is 2 eV.

| Generation | Particle | Mass [MeV] | Spin | Q/e |
|------------|----------|--------------------------|-------|--------|
| 1 | u | $2.2^{+0.6}_{-0.4}$ | $1/2$ | $+2/3$ |
| | d | $4.7^{+0.5}_{-0.4}$ | $1/2$ | $-1/3$ |
| 2 | c | 1270 ± 30 | $1/2$ | $+2/3$ |
| | s | 98^{+8}_{-4} | $1/2$ | $+2/3$ |
| 3 | t | $173210 \pm 510 \pm 710$ | $1/2$ | $+2/3$ |
| | b | 4180^{+40}_{-30} | $1/2$ | $-1/3$ |

Table 2.2: The mass, spin and electric charge (Q) of the quarks found in the Standard Model [10]. Each of the particles in the above table corresponds to three fermion fields, one for each of the three colours of the $SU(3)$ symmetry.

under a $SU(3)$, $SU(2)_L$ and $U(1)$ gauge transformations. The $SU(2)_L$ gauge symmetry acts on doublets formed of pairs of left handed chiral components of the fermion fields, $\psi_L = \frac{1}{2}(1 - \gamma_5)\psi$, while the right handed components, $\psi_R = \frac{1}{2}(1 + \gamma_5)\psi$, transform

trivially as singlets [11]. Similarly, the SU(3) symmetry acts on triplets formed of the fermion fields for each flavour of quark. All fields transform under the fundamental representation of U(1). The invariance of the Standard Model Lagrangian to these gauge transformations is established by introducing 12 gauge fields, summarised in table 2.3, through the covariant derivative of the fermion fields

$$\partial^\mu \rightarrow D^\mu = \partial^\mu + ig_1 Y B^\mu + ig_2 \mathbf{T} \cdot \mathbf{W}^\mu + ig_3 \mathbf{X} \cdot \mathbf{G}^\mu , \quad (2.3)$$

where B^μ is the gauge field for the U(1) symmetry, \mathbf{W}^μ ($W_j^\mu, j = 1, 2, 3$) are the fields of the SU(2)_L symmetry and \mathbf{G}^μ ($G_j^\mu, j = 1, \dots, 8$) are the fields of the SU(3). Y is the weak hypercharge, which relates to the chirality and flavour of the fermion field that it is associated to. The three coefficients g_1 , g_2 and g_3 are coupling constants related to the three gauged symmetry groups in the Standard Model. Mixing of the gauge fields for the U(1) and SU(2) symmetry of the form

$$Z_\mu = \cos\theta_W W_\mu^3 - \sin\theta_W B_\mu , \quad (2.4)$$

$$A_\mu = \sin\theta_W W_\mu^3 + \cos\theta_W B_\mu , \quad (2.5)$$

$$W_\mu^\pm = \frac{1}{\sqrt{2}}(W_\mu^1 \mp iW_\mu^2) , \quad (2.6)$$

where

$$\cos\theta_W = \frac{g_2}{g_1 + g_2} \text{ and } \sin\theta_W = \frac{g_1}{g_1 + g_2} , \quad (2.7)$$

gives the electroweak gauge bosons; W^\pm , Z and γ . This mixing ensures that the W^\pm and Z bosons become massive, while the γ remains massless. The G_j^μ fields are the eight massless gluons of the strong force. \mathbf{T} and \mathbf{X} are the generators for the SU(2) and SU(3) symmetries, which are typically chosen as

$$T_i = \frac{1}{2}\tau_i , \quad (2.8)$$

$$X_i = \frac{1}{2}\lambda_i , \quad (2.9)$$

$$(2.10)$$

where τ and λ are the Pauli and the Gell-Mann matrices respectively. The gauge fields

| Force | Particle | Mass [GeV] | Spin | Q/e |
|-----------------|---------------------------|----------------------|------|---------|
| Electromagnetic | γ | 0 | 1 | 0 |
| Weak Nuclear | W^\pm | 80.385 ± 0.015 | 1 | ± 1 |
| | Z | 91.1876 ± 0.0021 | 1 | 0 |
| Strong Nuclear | g ($\times 8$ colours) | 0 | 1 | 0 |
| Higgs | H | 125.1 ± 0.3 | 0 | 0 |

Table 2.3: The mass, spin and electric charge (Q) of the gauge bosons found in the Standard Model [10]. The γ and g_s theoretically have zero mass, which is consistent with measurements. The upper bound on the γ mass has been measured at 10^{-18} eV, while gluon masses of up to a few MeV have not been precluded. The upper bound on the magnitude of the charge of the γ is measured at 10^{-35} .

of the Standard Model, B_μ , \mathbf{W}_μ and \mathbf{G}_μ , transform under the gauge transformations as

$$K_\mu \rightarrow K'_\mu = UK_\mu U^\dagger + \frac{i}{g}(\partial^\mu U)U^\dagger , \quad (2.11)$$

where K_μ is any of B_μ , \mathbf{W}_μ and \mathbf{G}_μ and g is the coupling constants associated to the relevant gauged symmetry group. As the B_μ , \mathbf{W}_μ and \mathbf{G}_μ gauge fields are spin-1, they are described by the Proca Lagrangian density

$$\mathcal{L} = -\frac{1}{4}F_i^{\mu\nu}F_{\mu\nu i} + \frac{1}{2}m_K^2K_{i\mu}K_i^\mu , \quad (2.12)$$

where

$$F_i^{\mu\nu} = \partial^\mu K_i^\nu - \partial^\nu K_i^\mu - g f_{ijk} K_j^\mu K_k^\nu , \quad (2.13)$$

f_{ijk} are the fully anti-symmetric structure constants of the group, K_i^μ is the i^{th} gauge field of the group and m_K is a mass term for the gauge boson. The structure constants are defined from the commutation relations between generators of the symmetry group

$$[T_i, T_j] = i f_{ijk} T_k . \quad (2.14)$$

These structure constants govern the self-interactions for the gauge bosons. There is only one structure constant for the U(1) symmetry, which is zero, as the U(1) symmetry is abelian. The SU(2) symmetry structure constants are $f_{ijk} = \epsilon_{ijk}$, where ϵ_{ijk} is the Levi-Civita tensor. Due to the symmetries that are present in the Standard Model, $m_K = 0$ for all the gauge fields, however, it is clear that is is not the case. Therefore, to

generate gauge boson mass terms a Higgs field is introduced that undergoes spontaneous symmetry breaking, as described in section 2.2.

2.2 Higgs Physics

Mass terms are generated in the Standard Model by introducing a Higgs field that undergoes spontaneous symmetry breaking. This allows the gauge bosons, as well as the quarks and leptons, to obtain a mass, while still respecting the gauge symmetries found in the Standard Model.

2.2.1 Spontaneous Symmetry Breaking

To illustrate spontaneous symmetry breaking, consider a complex scalar field ψ with the Klein-Gordon Lagrangian

$$\mathcal{L} = \partial^\mu \psi^* \partial_\mu \psi - m^2 |\psi|^2 = \partial^\mu \psi^* \partial_\mu \psi - V(\psi) , \quad (2.15)$$

where m is a mass term and $V(\psi)$ is the potential the field ψ . This Lagrangian density is invariant under the global symmetry $\psi \rightarrow e^{i\alpha} \psi$. By adding extra terms to the Lagrangian, which retain the invariance to this global symmetry, it is possible to modify the interactions of this scalar field. For example, consider modifying the potential of the scalar field to the following

$$V(\psi) = m^2 |\psi|^2 + \lambda |\psi|^4 , \quad (2.16)$$

If $m^2 > 0$, the potential has a minima at zero, however, if $m^2 < 0$ then the minima exists on a circle in the complex ψ plane, which is centred at $(0, 0)$ and has radius $v = \sqrt{-m^2/\lambda}$. To quantise this theory it is necessary to expand about the minima of the potential. However, in the case of $m^2 < 0$ there are an infinite number of choices of minima to expand about. Irrespective of the choice of minima used to expand the field about, the symmetry $\psi \rightarrow e^{i\alpha} \psi$ is broken. Fluctuations about the minima along the degenerate direction leave the potential unchanged, which is a consequence of the breaking of the $\psi \rightarrow e^{i\alpha} \psi$ symmetry; this is known as spontaneous symmetry breaking. Goldstone's theorem [12] implies that, for Lorentz-invariant theories, spontaneous symmetry breaking always leads to the existence a massless particles known as Goldstone bosons. For

example, consider expanding the complex scalar ψ about the minima. In that case, ψ takes the form

$$\psi = \frac{1}{\sqrt{2}}(v + \psi_1 + i\psi_2) , \quad (2.17)$$

where ψ_1 and ψ_2 are real fields and $v = \sqrt{-m^2/\lambda}$. Applying this parameterisation to the Lagrangian yields a mass term of $\sqrt{-m^2}$ for the ψ_1 field. However, there is no corresponding mass term for the ψ_2 field, which indicates that it is massless as predicated by Goldstone's theorem

$$\mathcal{L} = \frac{1}{2}\partial^\mu\psi_1\partial_\mu\psi_1 + \frac{1}{2}\partial^\mu\psi_2\partial_\mu\psi_2 - m^2|\psi_1|^2 + \dots , \quad (2.18)$$

Spontaneous symmetry breaking is the origin of the gauge boson mass terms when applied to local symmetries instead of global ones. For example consider the global symmetry, $\psi \rightarrow e^{i\alpha}\psi$ that exists in equation 2.15. If this global symmetry is promoted to a local symmetry by letting $\alpha \rightarrow \alpha(x)$ and $\partial^\mu \rightarrow D^\mu = \partial^\mu + iA^\mu$, where A^μ is the gauge field that transforms as $A^\mu \rightarrow A^\mu - \partial^\mu\alpha(x)$, the Lagrangian becomes

$$\mathcal{L} = (D^\mu\psi)^*(D_\mu\psi) - m^2|\psi|^2 - \lambda|\psi|^4 . \quad (2.19)$$

If the ψ field is expanded about a non-zero minima in the potential, i.e. $m^2 < 0$ and $v = \sqrt{-m^2/\lambda}$, as was done in equation 2.17, then a gauge boson mass term, $+\frac{v^2}{2}A^\mu A_\mu$, is generated from the $(D^\mu\psi)^*(D_\mu\psi)$ term.

2.2.2 Electroweak Interactions

The electroweak sector of the Standard Model is that related to the $SU(2)_L \times U(1)$ symmetry [13]. In this sector, spontaneous symmetry breaking must occur in such a way as to give three massive gauge bosons, W^\pm and Z , and one massless gauge boson, the γ . This can be achieved through a Higgs field, H , that transforms as a doublet under the $SU(2)_L$ symmetry. The Lagrangian for this field is

$$\mathcal{L}_{Higgs} = (D_\mu H)^\dagger D^\mu H - V(H) . \quad (2.20)$$

The Higgs potential, $V(H)$, is

$$V(H) = -\mu^2 H^\dagger H + \lambda(H^\dagger H)^2 , \quad (2.21)$$

where μ and λ are constants. The covariant derivative of this Higgs field must satisfy the $SU(2)_L \times U(1)$ gauge symmetry meaning it takes the form

$$D_\mu H = (\partial_\mu + ig_1 Y B_\mu + ig_2 \frac{\tau^i}{2} W_\mu^i) H , \quad (2.22)$$

where g_1 and g_2 are coupling constants for the $U(1)$ and $SU(2)_L$ gauged symmetries respectively, $Y = \frac{1}{2}$ is the weak hypercharge of the Higgs and τ^i are the Pauli matrices. B_μ and W_μ^i are the gauge fields for the $U(1)$ and $SU(2)_L$ gauged symmetries respectively.

Consider spontaneously breaking the symmetry in the Higgs sector by expanding the Higgs field about a non-zero vacuum expectation value (vev)

$$\langle H \rangle = \begin{pmatrix} 0 \\ \frac{v}{\sqrt{2}} \end{pmatrix} , \quad (2.23)$$

where the minima of the field is defined as

$$\frac{v}{\sqrt{2}} = \sqrt{\frac{\mu^2}{2\lambda}} , \quad (2.24)$$

where v real. In that case, the kinematic term in the Higgs Lagrangian, $D^\mu H^\dagger D_\mu H$, contains mass terms for the gauge bosons

$$D^\mu H^\dagger D_\mu H \subset \frac{v^2}{2} (ig_1 Y B^\mu + ig_2 \frac{\tau^i}{2} W^{i\mu}) (ig_1 Y B_\mu + ig_2 \frac{\tau^i}{2} W_\mu^i) . \quad (2.25)$$

If there is mixing of the $SU(2)_L$ and $U(1)$ fields of the form

$$Z_\mu = \cos\theta_W W_\mu^3 - \sin\theta_W B_\mu , \quad (2.26)$$

$$A_\mu = \sin\theta_W W_\mu^3 + \cos\theta_W B_\mu , \quad (2.27)$$

$$W_\mu^\pm = \frac{1}{\sqrt{2}} (W_\mu^1 \mp i W_\mu^2) , \quad (2.28)$$

then the following gauge boson mass terms are generated

$$\frac{(gv)^2}{4} W_\mu^+ W^{-\mu} + \frac{(g^2 + g'^2)v^2}{8} Z_\mu Z^\mu . \quad (2.29)$$

The gauge boson masses generated by spontaneous symmetry breaking of the Higgs field are

$$\begin{aligned} m_W &= \frac{gv}{2}, \\ m_Z &= \frac{v\sqrt{g^2 + g'^2}}{2} = \frac{m_W}{\cos\theta_W}, \\ m_A &= 0, \end{aligned} \tag{2.30}$$

where θ_W is the Weinberg angle. This mixing produces a massless gauge boson, the γ , and three massive gauge bosons, the W^\pm and Z . By acquiring a non-zero vev, the Higgs field breaks the $SU(2)_L \times U(1)$ symmetry that was present in the Lagrangian to the $U(1)_{em}$ symmetry of electromagnetism.

The ratio of the masses of the W^\pm and Z bosons is predicted when spontaneous symmetry breaking occurs in the Higgs sector. This prediction sets the ρ parameter to unity, where the ρ parameter is defined as

$$\rho = \frac{m_W^2}{m_Z^2 \cos^2\theta_W} = 1. \tag{2.31}$$

This is a consequence of the Higgs potential containing custodial symmetry [10]. As the ρ parameter has been experimentally measured to be 1.00040 ± 0.00024 [14], it is clear that any extension to the Standard Model should retain this result.

2.2.2.1 Custodial Symmetry

The Standard Model Higgs field is defined by the Lagrangian

$$\mathcal{L}_{Higgs} = (D_\mu H)^\dagger D^\mu H - V(H), \tag{2.32}$$

where

$$V(H) = -\mu^2 H^\dagger H + \lambda (H^\dagger H)^2, \tag{2.33}$$

and μ and λ are constants. By construction, the Higgs sector of the Standard Model is invariant under local $SU(2)_L \times U(1)$ gauge transformations. However, a larger global

symmetry also exists in this sector, which can be seen by considering the Higgs doublet [15]

$$H = \begin{pmatrix} \psi^+ \\ \psi^0 \end{pmatrix} = \begin{pmatrix} \psi_1 + i\psi_2 \\ \psi_3 + i\psi_4 \end{pmatrix}. \quad (2.34)$$

All the terms in the Higgs potential involve $H^\dagger H = \psi_1^2 + \psi_2^2 + \psi_3^2 + \psi_4^2$, which is invariant under any rotation of these four components and hence under a $SO(4)$ global symmetry. In general, $SO(4) \cong SU(2) \times SU(2)$, where \cong denotes an isomorphism. In the case of the Higgs sector $SO(4) \cong SU(2)_L \times SU(2)_R$ where the $SU(2)_L$ symmetry is the gauged symmetry of the Standard Model. This symmetry can be manifested using an alternative parameterisation [16] of the Higgs field

$$\Phi = (i\tau_2 H, H) = \begin{pmatrix} \psi^{0*} & \psi^+ \\ -\psi^{+*} & \psi^0 \end{pmatrix}. \quad (2.35)$$

In this parametrisation the Higgs Lagrangian, \mathcal{L}_{Higgs} , becomes

$$\mathcal{L}_{Higgs} = \frac{1}{2} \text{Tr}[(D_\mu \Phi)^\dagger D^\mu \Phi] + \mu^2 \text{Tr}[\Phi^\dagger \Phi] - \lambda \text{Tr}[\Phi^\dagger \Phi \Phi^\dagger \Phi], \quad (2.36)$$

which is invariant under transformations of the form

$$\Phi \rightarrow U_L \Phi U_R^\dagger, \quad (2.37)$$

where U_L and U_R are transformations of the $SU(2)_L$ and $SU(2)_R$ symmetry groups respectively.

When the Higgs field acquires a non-zero vev the $SU(2)_L \times SU(2)_R$ symmetry of the Higgs potential is broken to a $SU(2)_C$ symmetry, which is known as custodial symmetry [17]. As $SO(3) \cong SU(2)$, symmetry breaking in the Higgs sector is equivalent to a $SO(4)$ symmetry being broken to a $SO(3)$ symmetry. This becomes clear when considering the form of the Higgs potential after symmetry breaking. Prior to symmetry breaking a $SO(4)$ global symmetry is present, however, after expanding the Higgs about a non-zero vev, defined in equation 2.23, the terms in the Higgs potential involve $H^\dagger H = (\psi_3 - v)^2 + \psi_1^2 + \psi_2^2 + \psi_4^2$, which is only invariant to rotations between the ψ_1 , ψ_2 and ψ_4 fields, which is a $SO(3)$ symmetry.

The Higgs field, H , transforms a singlet under this $SU(2)_C$ custodial symmetry, while the $SU(2)_L$ gauge boson fields, W_μ^i , transform as a triplet. It is the transformation of the

W_μ^i fields under the $SU(2)_C$ symmetry that enforces the relationship between the masses of the W^\pm and Z gauge bosons and that ρ should equal unity. It should be noted that the $SU(2)_L \times SU(2)_R$ symmetry only exists in the Higgs sector of the Standard Model. The $SU(2)_R$ symmetry in the Standard Model is broken by Yukawa couplings of the Higgs to quarks and leptons and by a non-zero coupling to the $U(1)$ gauge symmetry of the Standard Model, g_1 . However, this breaking of the $SU(2)_R$ symmetry is weak, which means the deviations of ρ from unity are minimal [17].

2.3 Effective Field Theory

There are a number of features in the observable universe that cannot be accounted for using the Standard Model of particle physics. However, the Standard Model is a very good description of the interactions between particles at the energies being probed at modern particle collider experiments. Any underlying theory governing the interactions of particles must, therefore, behave like the Standard Model over these energies, or distance scales. Above such energies the theory will deviate from the Standard Model to account for the full underlying theory. Effective field theories (EFTs) work from this premise by assuming that the complete theory has a momentum scale, Λ , below which Standard Model behaviour is replicated [18, 19].

Quantum field theories must be renormalizable to ensure that non-infinite predictions of the coefficients in the Lagrangian can be made and tested [20]. Infinities arise from non-renormalizable theories due to divergent integrals from loop diagrams that assume the theory being applied is valid at all energy and length scales. Effective field theories act to avoid such problems by only integrating up to the momentum scale Λ and not above it. At the energy scale being considered, any infinities arising from the loop calculations in the EFT can be absorbed into a finite number of parameters. This methodology avoids the assumption that the theory in question is applicable to all energy scales and allows measurable predictions to be made.

As the Standard Model should be replicated at the low energy scale, it is appropriate when creating an EFT Lagrangian to append new operators to the Standard Model Lagrangian to account for areas of new physics. This gives the general form for an EFT

Lagrangian as [18]

$$\mathcal{L}_{EFT} = \mathcal{L}_{SM} + \sum_{\text{dimension } d>4} \sum_i \frac{c_i^{(d)}}{\Lambda^{d-4}} \mathcal{O}_i^{(d)}, \quad (2.38)$$

where \mathcal{L}_{SM} is the Standard Model Lagrangian, $c_i^{(d)}$ are free parameters, $\mathcal{O}_i^{(d)}$ is the i^{th} unique operator with dimension d in the EFT and Λ is the EFT momentum scale. The sum runs over all unique operators with dimension greater than four. The presence of the Λ^{d-4} in the denominator is required to ensure correct dimensionality of the new terms being added to the Lagrangian.

New physics is introduced by the operators $\mathcal{O}_i^{(d)}$, but suppressed by the momentum scale Λ . It is assumed that Λ is large with respect to the momentum scales that have been examined at preexisting particle collider experiments, therefore, any new physics is suppressed. Under this assumption, new operators with dimension less than, or equal to, four can be vetoed from the EFT as their effects would be readily observed at preexisting particle collider experiments, due to the Λ^{4-d} coefficient. At energies below the momentum scale, Λ , it is possible to find the dominant new physics terms in the EFT and consider these as corrections to the Standard Model. Above this scale the EFT breaks down as operator $\mathcal{O}_i^{(d)}$ in \mathcal{L}_{EFT} has a non-negligible coefficient. In the extremal limit, $\Lambda \rightarrow \infty$, the Standard Model is recovered as new physics is too far out of reach to have any impact on observables.

2.4 Electroweak Chiral Lagrangian

The introduction of a Higgs field undergoing spontaneous symmetry breaking is able to produce mass terms in the Lagrangian for the W^\pm and Z bosons. However, it is possible to introduce these terms by parameterising the Higgs field using the gauge boson fields of the $SU(2)_L$ Standard Model symmetry [21]. In this approach, the pattern of spontaneous symmetry breaking mirrors that found in the Higgs sector of the Standard Model i.e. a global $SU(2)_L \times SU(2)_R$ symmetry is broken to a $SU(2)_C$ symmetry. This will ensure that the ρ parameter, introduced in section 2.2.2, retains a value of unity, which is consistent with experimental measurements. The Standard Model spontaneous symmetry breaking pattern can be replicated using a field, $\Sigma(x)$, which transforms under

the $SU(2)_L \times SU(2)_R$ global symmetries as

$$\Sigma \rightarrow U_L \Sigma U_R^\dagger , \quad (2.39)$$

where U_L and U_R are transformations of the $SU(2)_L$ and $SU(2)_R$ symmetry groups respectively and $\Sigma(x)$ is

$$\Sigma(x) = \exp\left(\frac{-i}{v} \sum_{a=1}^3 \pi^a \tau^a\right) , \quad (2.40)$$

where π^a are the three would-be Goldstone bosons that exist when the $SU(2)_L \times U(1)$ symmetry is broken to $U(1)_{em}$ [22]. The $SU(2)_L$ and $U(1)$ symmetries of the Standard Model are gauged in the usual way by defining the covariant derivative of the Σ field

$$\mathcal{D}_\mu \Sigma(x) = \partial_\mu \Sigma(x) + \frac{ig_2}{2} W_\mu^a \tau^a \Sigma(x) - \frac{ig_1}{2} B_\mu \tau^3 \Sigma(x) , \quad (2.41)$$

where g_1 and g_2 are coupling constants for the $U(1)$ and $SU(2)_L$ symmetries respectively and τ^a are the Pauli spin matrices. The lowest order derivative term for this Σ field that could appear in the Lagrangian is

$$\mathcal{L}_\Sigma = \frac{v^2}{4} \text{Tr}(\mathcal{D}^\mu \Sigma^\dagger \mathcal{D}_\mu \Sigma) = -\frac{v^2}{4} \text{Tr}(V_\mu V^\mu) , \quad (2.42)$$

where $V_\mu = (\mathcal{D}_\mu \Sigma) \Sigma^\dagger$. This term respects all the symmetries present in the Higgs sector of that Standard Model, including the custodial symmetry in the limit $g_1 \rightarrow 0$. Furthermore, by expanding this field about a non-zero vev, the $SU(2)_L \times SU(2)_R$ global symmetry is broken to a $SU(2)_C$ symmetry exactly as it is in the Standard Model. For example, if this field is expanded about the point $\Sigma = \mathbb{1}$, i.e. the unitary gauge, mass terms for the electroweak gauge bosons are generated that match those produced from spontaneous symmetry breaking of the Higgs field as described in section 2.2.1

$$\frac{v^2}{4} \text{Tr}[V^\mu V_\mu] = -\frac{(gv)^2}{4} W_\mu^+ W^{-\mu} - \frac{(g^2 + g'^2)v^2}{8} Z_\mu Z^\mu \quad (2.43)$$

$$\begin{aligned} m_A &= 0 , \\ m_W &= \frac{gv}{2} , \\ m_Z &= \frac{v\sqrt{g^2 + g'^2}}{2} = \frac{m_W}{\cos\theta_W} , \end{aligned} \quad (2.44)$$

So far, all that has been done is a parameterisation of the Higgs field, however, it was shown by Longhitano [22] that there are several relevant operators involving the Σ field that are $SU(2)_L \times U(1)$ invariant. As these operators obey the same symmetries as those found in the Standard Model they should be considered. This can be done using EFT approach, as discussed in section 2.3. Of the operators introduced by Longhitano, only two involve quartic massive gauge boson vertices and preserve the custodial symmetry [23]. They are

$$\alpha_4 \text{Tr}[V^\mu V_\nu] \text{Tr}[V^\nu V_\mu] \quad \text{and} \quad \alpha_5 \text{Tr}[V^\mu V_\mu]^2. \quad (2.45)$$

These terms contribute to the massive gauge boson quartic vertices shown in figure 2.1. The Standard Model already contains triple and quartic vertices involving the electroweak gauge bosons, shown in figure 2.2, and these are also present in this EFT approach. These vertices originate from the kinematic terms in the Proca Lagrangian density $\mathcal{L}_{kin} = -\frac{1}{4}B_{\mu\nu}B^{\mu\nu} - \frac{1}{4}W_{\mu\nu}W^{\mu\nu}$. Of the vertices showing sensitivity to α_4 and α_5 , only that shown in figure 2.1c is not present in the Standard Model.

Both terms shown in equation 2.45 contain dimension 8 operators [18] and, with respect to the EFT approach, i.e. equation 2.38, their coefficients are proportional to Λ^{-4} , where Λ is the momentum scale of the new physics being modelled. In the limit that the momentum scale of new physics is beyond experimental reach, i.e. $\Lambda \rightarrow \infty$, these terms do not contribute to measurable observables and the Standard Model is recovered. It should be noted that in this case, the Standard Model has been parameterised using the Σ field, so in the limit $\Lambda \rightarrow \infty$, the gauge boson mass terms generated from \mathcal{L}_Σ do not vanish.

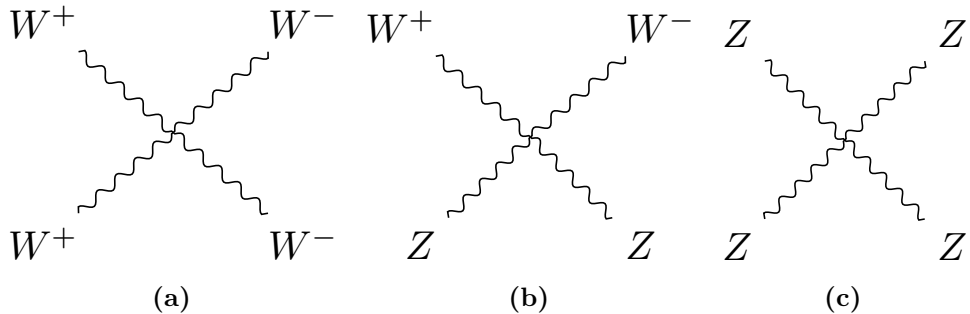


Figure 2.1: Gauge boson self-coupling vertices that are sensitive to the anomalous gauge couplings α_4 and α_5 .

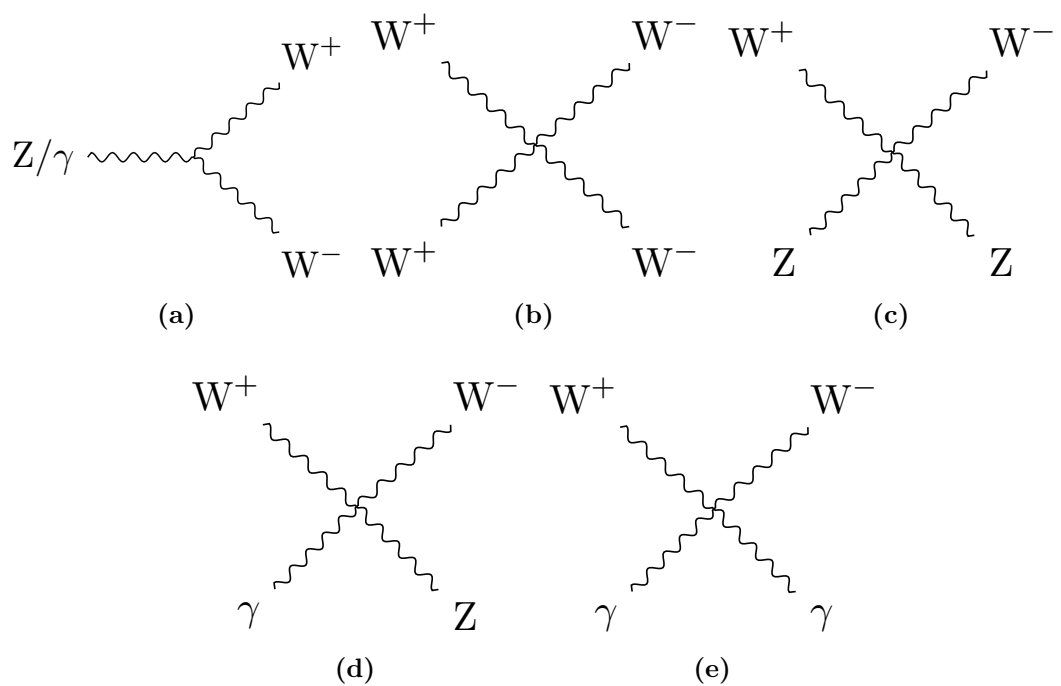


Figure 2.2: Gauge boson self-coupling vertices in the Standard Model.

Chapter 3

Particle Flow Calorimetry for Future Linear Colliders

“I am fond of pigs. Dogs look up to us. Cats look down on us. Pigs treat us as equals.”

— Winston Churchill

Particle flow calorimetry can provide extremely good jet energy resolutions at a future linear collider. Jet energy resolution is crucial at the linear collider as many of the interesting processes will be characterised by multi-jet final states. Many of these multi-jet final states will be produced from the hadronic decays of W and Z bosons and one of the key goals of the future linear collider is to be able to separate these decays. Separation of these decays can be achieved, however, only by placing a tight requirement on the jet energy resolution; $\sigma_E/E \lesssim 3.5\%$ for 50-500 GeV jets at the ILC and up to 1.5 TeV at CLIC [24]. The use of particle flow calorimetry will also be highly beneficial for quantifying final states of interest that involving charged leptons and missing momentum.

3.1 Particle Flow Calorimetry

The premise of particle flow calorimetry is to use the sub-detector that offers the best energy resolution to measure the energy of any given particle, which corresponds to energy measurements being made in the ECal for γ s, the HCal for neutral hadrons and, crucially, the tracker for charged particles. The starker contrast of this approach to that

of traditional calorimetry occurs in the measurement of the energy of charged particles. In particle flow calorimetry the energy of a charged particle is measured using the curvature of the path it transverses as it bends in a magnetic field, while in traditional calorimetry the energy would be measured using the calorimeters, predominantly the hadronic calorimeter (HCal). The tracker energy resolution for a single charged particle of energy E_{X^\pm} is typically $10^{-4} \times E_{X^\pm}^2$, while for the HCal it is $\sim 0.55 \times \sqrt{E_{X^\pm}}$ [24]. The energy resolution offered by the tracker is significantly better than that offered by the HCal for energies up to $\sim \mathcal{O}(300 \text{ GeV})$. This means that particle flow calorimetry has the potential to offer a much better energy resolution for charged particles below $\sim \mathcal{O}(300 \text{ GeV})$, than that of the traditional calorimetry approach. Particle flow calorimetry offers gains in performance for collision energies well beyond 300 GeV as the average long-lived particle energy for physics processes of interest is typically much less than 300 GeV. Furthermore, it also leads to a significant improvement in the measurement of jet energies as, after the decay of short-lived particles, approximately 60% of the energy of a jet is carried in the form of charged particles. The measurement of jet energies in the particle flow paradigm is summarised in table 3.1. The benefits to the energy resolution, for both charged particles and jets, offered by the particle flow approach to calorimetry is the driving factor behind why it is planned for used at the linear collider experiment.

| Jet Component | Detector | Energy Fraction | Energy Resolution |
|-------------------------------|----------|-----------------|-------------------------------|
| Charged Particles (X^\pm) | Tracker | $\sim 0.6E_j$ | $10^{-4} \times E_{X^\pm}^2$ |
| Photons (γ) | ECal | $\sim 0.3E_j$ | $0.15 \times \sqrt{E_\gamma}$ |
| Neutral Hadrons (X^0) | HCal | $\sim 0.1E_j$ | $0.55 \times \sqrt{E_{X^0}}$ |

Table 3.1: The approximate jet fractions and energy resolutions for charged particles (X^\pm) of energy E_{X^\pm} , photons (γ) of energy E_γ and neutral hadrons (X^0) of energy E_{X^0} . The energy resolution for photons and neutral hadrons reflects the performance of a linear collider like ECal and HCal respectively. Taken from [24].

Particle flow calorimetry is challenging to put into practice as it requires a precise reconstruction for all long-lived particles within a detector. Charged particle energy measurements are made using the curvature of the track they transverse as they bend in the magnetic field, but they also produce calorimetric energy deposits, as shown in figure 3.1. If both of these energy measurements are used, the energy of all charged particles would be double counted. Therefore, to avoid this, any calorimetric energy deposits originating from charged particles are not included in the final energy measurement. However, this

methodology makes it possible to double count and omit energy measurements if the origin of a calorimetric energy deposit is misidentified. For example:

- If a calorimetric energy deposit, made by a charged particle, is not associated to a track, the calorimetric energy deposit will be double counted: Firstly, when the track energy is accounted for and secondly, when the calorimetric energy deposit is incorrectly reported as the energy of a neutral particle.
- If a calorimetric energy deposit, made by a neutral particle, is incorrectly associated to a track, that calorimetric energy deposit is not accounted for.

These effects, collectively known as "confusion", degrade the energy resolution of a particle flow detector. Therefore, it is crucial to make correct associations between charged particle tracks and their calorimetric energy deposits to minimise the effect of confusion. These associations can only be successfully made if the calorimeters used have fine segmentation, such as those found at the linear collider experiment, so that it becomes possible to separate the energy deposits from nearby showering particles. Even with this segmentation, making the association of charged particle tracks to calorimetric energy deposits is highly non-trivial. At the linear collider experiment, these associations are made using sophisticated pattern recognition algorithms, provided by PandoraPFA. The fine segmentation of the linear collider calorimeters allows PandoraPFA to reconstruct the four-momenta of all particles passing through the detector and to report the energy of all reconstructed particles using energy measurements from the optimal sub-detectors.

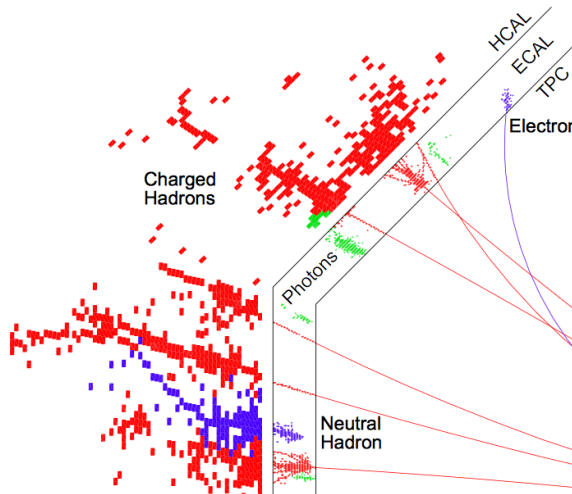


Figure 3.1: A typical simulated 250 GeV jet in the CLIC_ILD detector, with labels identifying constituent particles. Image taken from [25].

3.2 International Large Detector

The current detector concepts for the linear collider experiments have been designed to make particle flow calorimetry possible. While there are a number of different concepts that are under consideration for both the ILC and CLIC, one of the most prominent, and the focus of this work, is the International Large Detector (ILD). The ILD detector, shown in figure 3.2, achieves very high spatial resolution for all sub-detector systems thanks to its highly segmented calorimeters and central tracking system, both of which are encompassed within a 3.5 T magnetic field. The sophisticated pattern recognition software that is needed for particle flow calorimetry is provided by PandoraPFA [24, 25].

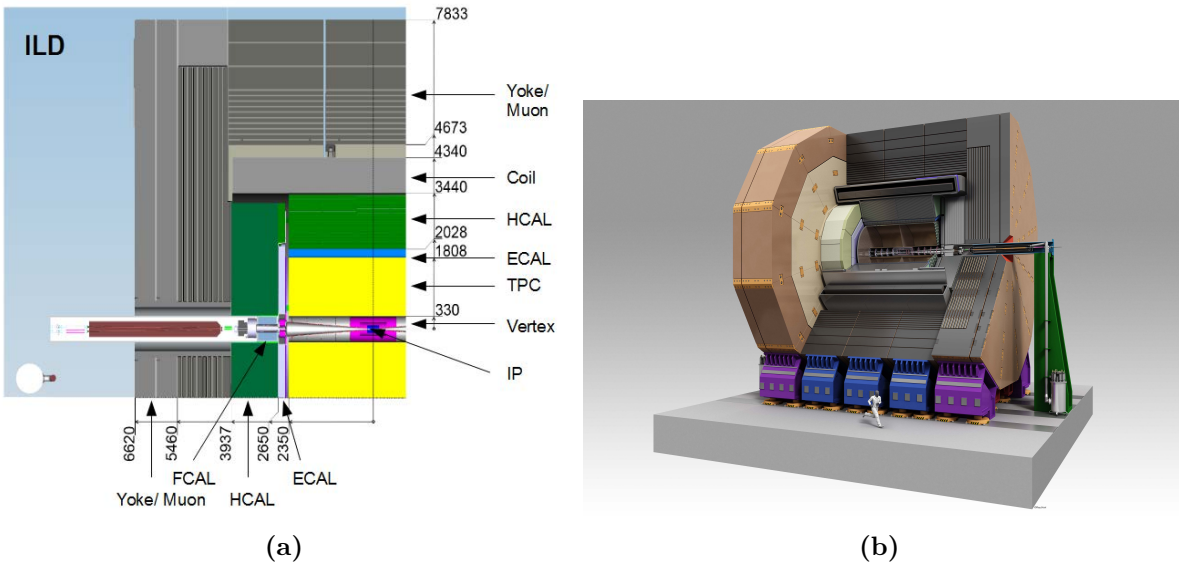


Figure 3.2: (a) Quadrant view of the ILD detector concept. The interaction point is in the lower right corner of the picture. Dimensions are in mm. (b) An artistic view of the ILD detector concept. Figures taken from [26].

3.2.1 Overview

The tracking system for the ILD detector consists of a vertex detector, a Time Projection Chamber (TPC) and a number of supplementary silicon detectors. The vertex detector is designed to give precise information about displaced vertices with respect to the impact point (IP), which is crucial for the study of short lived particles such as the D and B mesons. The vertex detector is located close to the IP and surrounding it is the TPC, which is the central tracker for ILD. The TPC provides detailed measurements of the

trajectory of charged particle tracks passing through it, up to 224 measurements per track. This information is used for determining the curvature of the charged particle track and hence the momentum of the charged particle that transversed it. Finally, the purpose of the supplementary silicon detectors is to provide additional, high precision, spatial measurements to aid track fitting and extend coverage of the detector down to low polar angles.

The calorimetric system for ILD is comprised of an electromagnetic calorimeter (ECal), a hadronic calorimeter (HCal) and a number of forward calorimeters (FCal). The primary function of the ECal is to induce electromagnetic particles to shower within it and to measure the energy of these particle showers. Similarly, the HCal is designed to induce and measure the energy of hadronic particle showers. The ECal surrounds the tracking system in the ILD detector and is itself surrounded by the HCal. The function of FCal is to extend the coverage of the calorimeter system to low polar angles and to provide measurements of the luminosity of the colliding e^\pm beams.

The outermost elements of the ILD detector are the solenoid, iron yoke and muon system. The solenoid generates a magnetic field of 3.5 T, which is essential for determining the energy of charged particles in the particle flow paradigm. The iron yoke is used to return the magnetic field generated by the solenoid. The yoke is instrumented by the muon system to provide additional information, which supplements the calorimetric energy measurements made by the ILD calorimeters.

3.2.2 Vertex Detector

The main goal of the ILD vertex detector is to achieve a resolution on the impact parameter of charged particle tracks of

$$\sigma_b < 5 \oplus \frac{10}{p \sin(\theta)^{3/2}} \mu\text{m}, \quad (3.1)$$

where σ_b is the resolution on the track impact parameter, p is the momentum of the track and θ is the angle between the track and the vertex detector plane. The first term in this parameterisation is the transverse impact parameters resolution and the second is a multiple-scattering term. This makes precisely tagging secondary vertices from charm and bottom mesons possible. Typically these mesons have relatively short proper lifetimes, τ , such that $c\tau \approx \mathcal{O}(300 \mu\text{m})$. To achieve this impact parameter resolution, a spatial resolution of better than 3 μm is required near the impact point (IP). Furthermore, a

low material budget of less than 0.15 % of a radiation length per layer is required to ensure that few electromagnetic showers are initiated within the vertex detector. A low pixel occupancy is essential for determining the trajectory of individual tracks in the detector. Furthermore, consideration will have to be given to the mechanical structure of the detector, power consumption and cooling.

There are a number of different pixel technology options under consideration for the vertex detector for the ILD detector. This is an active area of ongoing research and development for the linear collider collaboration. The current design of the vertex detector consists of three concentric layers of double-sided ladders with the first layer contains 10 ladders, the second 11 ladders and the third 17 ladders as shown in figure 3.3. Each ladder has two silicon pixel sensors on each side and the ladder thickness is approximately 2 mm. The radii covered by the detector range from 16 mm to 60 mm from the IP.

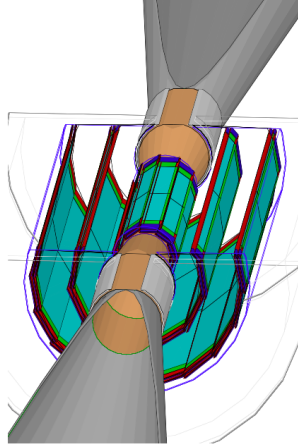


Figure 3.3: Vertex detector design for ILD. Figures taken from [27].

3.2.3 Time Projection Chamber

The central tracking system for the ILD detector is a TPC, which is shown in figure 3.4. The TPC consists of a cylindrical gas volume with a central electrode providing an axial electric field. When a charged particle passes through the TPC, it ionises the gas and the ionised molecules drift in the axial electric field. The direction of the electric field is chosen such that the electrons drift towards the endplates where they are collected. The position of the ionisation point can then be calculated using the drift time of the electrons in the TPC. Combining these TPC hits together makes reconstruction of the

full charged particle track possible. TPCs have an advantage over silicon tracking in that they continuously track any charged particle passing through them, while silicon detectors are only sensitive within each silicon layer. This compensates for the worse single point resolution that TPCs have in comparison to silicon detectors and makes TPCs a viable option for the ILD detector. Furthermore, TPCs have a very low material budget. This benefits calorimetry as it minimises energy losses prior to the particle energy entering the calorimeters, which means the calorimetric energy deposits give a better reflection of the true particle energy.

The ILD TPC has a point resolution of better than $100\ \mu\text{m}$ and a double hit resolution in ϕ of less than 2 mm. The gas used for the TPC will be Ar:CH₄:CO₂ (95:3:2) [28]. Several readout technology options, designed to measure the ionisation current, are currently under development. For all potential options it is envisaged that the readout pads would be $\approx 1 \times 6\text{mm}^2$ giving a total of approximately 10^6 pads on each TPC endplate.

3.2.4 Supplemental Silicon Tracking System

There are four components that make up the supplemental silicon tracking system in ILD, shown in figure 3.5, which are:

- Silicon Inner Tracker (SIT) and Silicon External Tracker (SET). These are both barrel components, which are positioned immediately inside and outside the TPC. The SIT helps form associations between hits in the vertex detector and TPC, while the SET helps with extrapolation of TPC tracks into the calorimeter.
- Endplate of the TPC (ETD). This sensor is identical to the SET, but is positioned in front of the ECal endcap calorimeter. The ETD extends the coverage of the supplemental silicon tracking system envelope.
- Forward tracker (FTD). This detector consists of seven silicon disks that extend the coverage of the tracking down to small angles that are not covered by the TPC.

The coverage of the SIT, SET, ETD and FTD is given in table 3.2. These detectors are designed to give high precision space points that can be used in track fitting. Furthermore, the ETD and SET are of particular use for extrapolating the charged particle tracks into the calorimeters. This is key for particle flow calorimetry, which relies upon correct

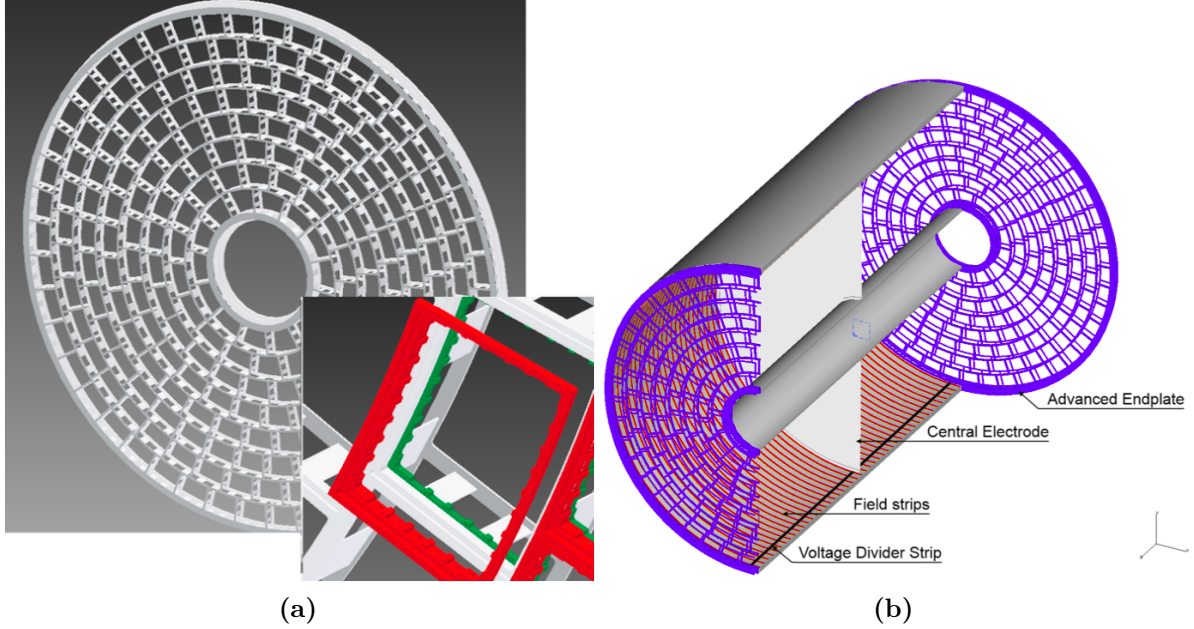


Figure 3.4: (a) Drawing of the proposed end-plate for the TPC. In the insert a back frame, which is designed to support the readout modules, is shown. (b) Conceptual sketch of the TPC system showing the main parts of the TPC (not to scale). The central electrode generates the axial electric field, the endplates collect the ionisation electrons, the field strips help to maintain a uniform electric field across the TPC and the voltage divider strips maintains the voltage difference between the anode and cathode. The field strips are held at fixed voltages such that they replicate the electric field produced by the electrodes. This reinforcing of the electric field configuration minimises non-uniformities in the electric field. The field cage of the TPC is not shown.

| Tracking System | Coverage [$\cos\theta$] |
|-----------------|---------------------------|
| SIT | 0.910 |
| SET | 0.789 |
| ETD | 0.799 - 0.985 |
| FTD | 0.802 - 0.996 |

Table 3.2: Coverage of the supplementary silicon tracking systems in the ILD detector. In this table θ is the polar angle with respect to the beam direction. Taken from [26].

association of charged particle tracks and clusters of calorimeter hits. Analogously to the vertex detector, these detectors require low material budget and low occupancy. The FTD, due to its proximity to the beam axis, is particularly prone to high occupancies.

The SIT, SET and ETD are silicon pixel sensors with $50 \mu\text{m}$ pitch embedded in $200 \mu\text{m}$ thick silicon. The FTD consists of seven silicon tracking disks, the first two being

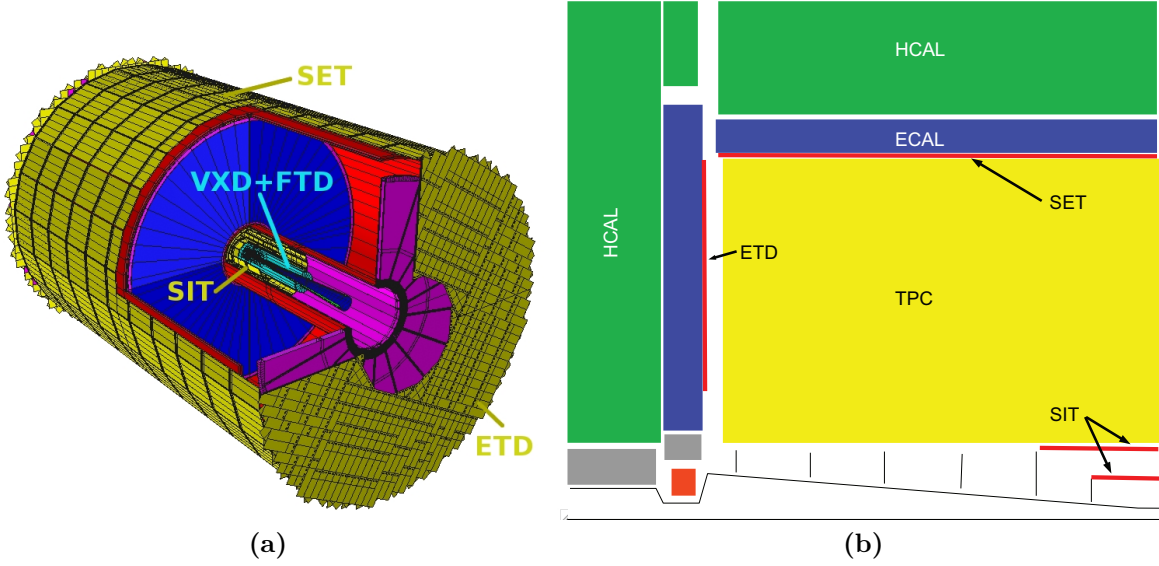


Figure 3.5: (a) A 3D detailed GEANT4 simulation description of the silicon system. (b) A quadrant view of the ILD silicon envelope made of the four components SIT, SET, ETD and FTD as included in the full MOKKA simulation. Figures taken from [26].

pixel detectors and the remaining five being strip detectors. The pixel detector disks are formed of 16 petals, as shown in figure 3.6. Within these petals the pixel size varies from $26 \times 29 \mu\text{m}^2$ to $26 \times 67 \mu\text{m}^2$. Strip detectors are used for the outermost tracking disks as the occupancy considerations do not demand a high granularity detector i.e. a pixel detector. These detector disks will have a pitch of $50 \mu\text{m}$. The active sensor and readout ASIC design for each of these detectors is an active area of development for the linear collider.

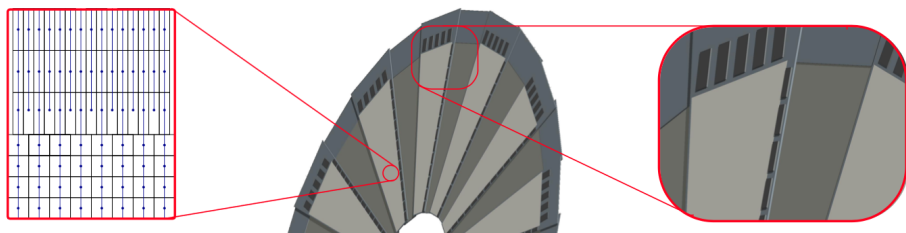


Figure 3.6: A half-disk for the FTD showing the petal concept. The rightmost zoom image shows a detail of the end-of-petal area that houses the read-out electronics. The leftmost image shows the region at $R = 8 \text{ cm}$ where both the column width and the R -dimension of the pixels changes. Figures taken from [26].

3.2.5 Electromagnetic Calorimeter

The nominal ILD detector contains a finely segmented electromagnetic sampling calorimeter (ECal). The ILD ECal has been specifically designed with particle flow calorimetry in mind. To that extent the spatial resolution of particle showers within the ECal takes as much, if not more, precedence than the energy resolution.

There are a number of design requirements for the ECal:

- The ECal must be compact in size to reduce the overall cost of the detector.
- Fine segmentation of the ECal is required so that nearby particle showers can be separated. This is an essential requirement for particle flow calorimetry.
- Electromagnetic showers should be contained within the ECal.

Based on these requirements tungsten is used as the absorber material for the ILD ECal as it has a small radiation length (X_0), a small Moli  re radius and a large ratio of radiation length to nuclear interaction length. A comparison of these properties for other ECal absorber material candidates is shown in table 3.3. The small radiation length in tungsten allows for a large number of radiation lengths, $\approx 24X_0$, to be compacted within a relatively short distance, ≈ 20 cm, in nominal ILD ECal. This is sufficient for containing all but the highest energy electromagnetic showers. The small Moli  re radius in tungsten will lead to compact electromagnetic showers. This makes separation of nearby showers easier. Finally, the large ratio of the radiation length to the nuclear interaction length in tungsten will lead to greater longitudinal separation between electromagnetic and hadronic showers again making shower identification easier.

The active material in the nominal ILD ECal is silicon, however, a scintillator strip option is also being considered. It contains a total of 30 longitudinal readout layers, which is sufficient to provide a good energy resolution. The tungsten thickness for the innermost 20 layers is 2.1 mm, while for the final 10 layers it is 4.2 mm. This configuration of absorber material thickness is chosen to reduce the number of readout channels and hence the cost, while maintaining a high sampling rate for particle showers at the start of the ECal. It should be noted that this ECal offers no gains in terms of energy resolutions in comparison to preexisting particle collider experiments, as shown in table 3.4. This is the case because the focus of this calorimeter is split between imaging the particle showers and recording their energy as opposed to purely focusing on the energy measurement. Each of the ECal layers is divided up into square cells, of side length 5 mm, which makes

separation of nearby particle showers possible. This cell size was chosen as a balance between being able to resolve nearby particle showers and reducing the overall cost of the calorimeter, which scales with the number of readout channels. An optimisation study of the various ECal parameters for the ILD detector can be found in section ??.

| Material | λ_I (cm) | X_0 (cm) | ρ_M (cm) | $\frac{\lambda_I}{X_0}$ |
|----------|------------------|------------|---------------|-------------------------|
| Fe | 16.8 | 1.76 | 1.69 | 9.5 |
| Cu | 15.1 | 1.43 | 1.52 | 10.6 |
| W | 9.6 | 0.35 | 0.93 | 27.4 |
| Pb | 17.1 | 0.56 | 1.00 | 30.5 |

Table 3.3: Comparison of the nuclear interaction length λ_I , radiation length X_0 and Moliére radius for iron, copper, tungsten and lead. Table taken from [24].

| Experiment | Ecal Energy Resolution $\frac{\sigma_E}{E}$ |
|-------------------------------|--|
| CMS [29] | $\sim \frac{2.8\%}{\sqrt{E(\text{GeV})}} \oplus 0.3\% \oplus \frac{12\%}{E(\text{GeV})}$ |
| ATLAS [30] | $\sim \frac{10.1\%}{\sqrt{E(\text{GeV})}} \oplus 0.1\%$ |
| LHCb [31] | $\sim \frac{9\%}{\sqrt{E(\text{GeV})}} \oplus 0.8\%$ |
| ILC (ILD Silicon Option) [26] | $\sim \frac{16.6\%}{\sqrt{E(\text{GeV})}} \oplus 1.1\%$ |

Table 3.4: Comparison of the ECal energy resolutions for various experiments.

3.2.6 Hadronic Calorimeter

A finely segmented hadronic sampling calorimeter (HCal) is used in the nominal ILD detector. The design requirements for the ILD HCal mirror those of the ECal, which can be found in section 3.2.5, with one exception; the HCal is designed to contain hadronic showers as opposed to electromagnetic showers. Steel is used as the absorber material for the HCal as it has durable mechanical properties that allow the HCal to be constructed without the need of auxiliary supports. If required, auxiliary supports would create dead regions in the detector that would harm performance. Furthermore, steel is relatively inexpensive and has a relatively small nuclear interaction length, meaning it is possible to achieve a compact calorimeter design at low cost. The nominal ILD HCal contains

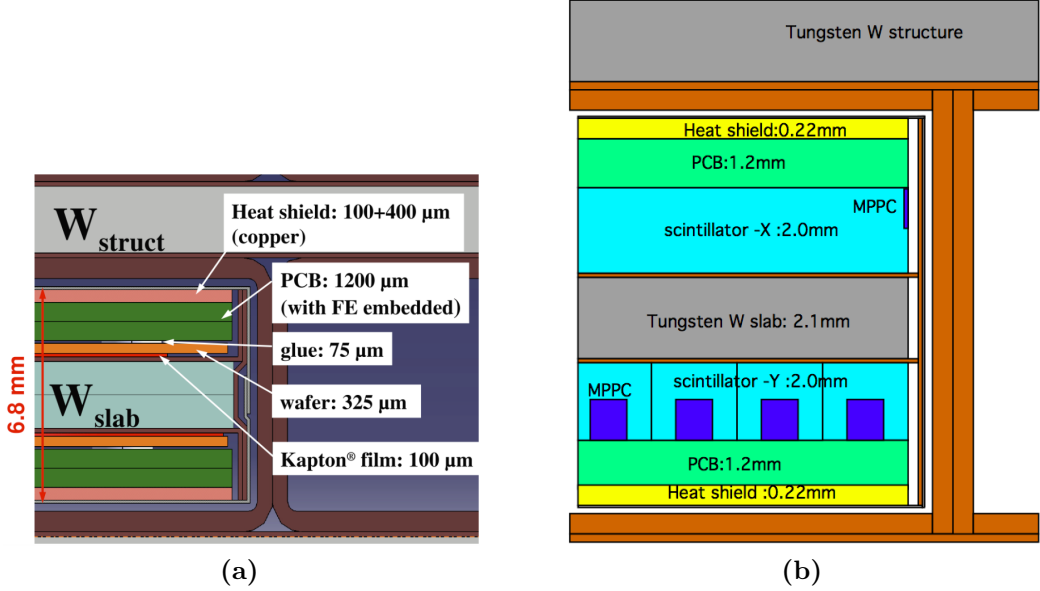


Figure 3.7: Cross section through ECal layer for (a) silicon and (b) scintillator option. Figures taken from [26].

approximately $6\lambda_I$, which when combined with the $1\lambda_I$ in the ECal is enough to contain the majority of hadronic showers at ILC like energies.

The active material in the nominal ILD HCal is scintillator. In total, the HCal contains 48 readout layers, which provides an extremely good energy resolution. This can be seen when comparing the HCal energy resolution between different experiments, as shown in table 3.5. An individual layer in the HCal is comprised of 20 mm of steel absorber material with 3 mm of scintillator active material. Each layer in the HCal is segmented into square cells, of side length 30 mm. This cell size was chosen as a balance between reducing the cost of the detector, which is proportional to the number of readout channels, and achieving the required spatial resolution to make particle flow calorimetry possible. The segmentation of the ILD HCal gives excellent spatial resolution and sufficiently good energy resolution to make the use of particle flow calorimetry a reality. An optimisation study of the various HCal parameters for the ILD detector can be found in section ??.

The ILD HCal is intrinsically non-compensating, which means that it has a different response to electromagnetic and hadronic showers. The origin of this different response is the fundamentally different mechanisms governing the propagation of electromagnetic and hadronic showers. One key difference between the mechanisms is that hadronic showers have an invisible energy component, which occurs due to effects such as neutrons

coming to rest in the detector and nuclear biding energy losses [32]. In general, this leads to a lower response from a calorimeter to a hadronic shower than an electromagnetic shower. A number of different software techniques have been developed for the linear collider experiment that attempt to correct this non-compensating response. For more details see chapter ???. The ILD ECal has a compensating response due to the use of tungsten as the absorber material [33], therefore, no additional treatment of energies is required.

| Experiment | HCal Energy Resolution $\frac{\sigma_E}{E}$ |
|-------------------------------|--|
| CMS [34] | $\sim \frac{90\%}{\sqrt{E(\text{GeV})}} \oplus 4.8\%$ |
| ATLAS [35] | $\sim \frac{52.1\%}{\sqrt{E(\text{GeV})}} \oplus 3.0\% \oplus \frac{1.6\%}{E(\text{GeV})}$ |
| LHCb [31] | $\sim \frac{69\%}{\sqrt{E(\text{GeV})}} \oplus 9.0\%$ |
| ILC (ILD Silicon Option) [26] | $\sim \frac{43.3\%}{\sqrt{E(\text{GeV})}} \oplus 1.8\%$ |

Table 3.5: Comparison of the HCal energy resolutions for various experiments.

3.2.7 Solenoid, Yoke and Muon System

Surrounding the ILD calorimeter system is solenoid that generates a 3.5 T magnetic field. The magnetic field produced by the coil is crucial for bending charged particles so that their momentum can be determined from the curvature of the path they transverse. Furthermore, the bending of charged particles leads to greater separation of calorimetric energy deposits between charged and neutral particles, which will reduce the effects of confusion when using particle flow calorimetry.

The magnetic field in the ILD detector is returned by an iron yoke that surrounds the solenoid. Iron is chosen for the yoke material as it has a very large permeability.

This yoke is instrumented by a muon system in the barrel and forward regions of the detector. The goal of this instrumentation is to identify muons escaping the calorimeters and to act as a tail catcher for the calorimeters. The muon system consists of 10 layers, spaced 140 mm apart, followed by 2 (3) layers spaced 600 mm apart in the barrel (endcap) region of the detector, as shown in figure 3.8. There is also an additional sensitive layer for the barrel region placed immediately outside the HCal to help with association energy deposits between the calorimeters and the yoke. As the majority of particles at ILC like

energies will be contained within the calorimeters, the energy and spatial resolution of the muon system are not critical to performance. It is for that reason that the number of layers is lower and the layer thicknesses wider in the yoke than in the calorimeters. The nominal ILD model uses 30 mm wide and 1 m long scintillator strips as the readout technology for the yoke.

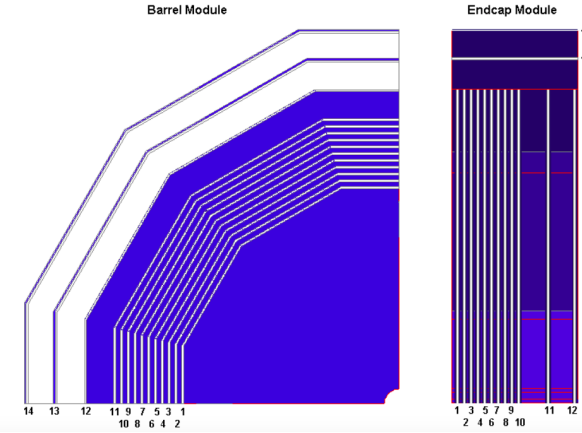


Figure 3.8: The sensitive layers of the ILD muon system. Figure taken from [26].

3.2.8 Forward Calorimetry

Forward calorimetry in the ILD detector consists of three additional sampling calorimeters:

- The LumiCal, which is located within the octagonal hole in the ECal endcap. This will give a precise measurement of the luminosity of the linear collider beam. The LumiCal uses Bhabha scattering, $e^+e^- \rightarrow e^+e^-(\gamma)$, as a gauge process for the luminosity measurement. Using this approach the luminosity can be measured with precision of less than 10^{-3} at $\sqrt{s} = 500$ GeV [28].
- The LHCAL, which is positioned within the square hole of the HCal endcap. This hadronic calorimeter is designed to extend the coverage of the HCal down to small polar angles.
- The BeamCal, which is located just in front of the final focusing quadrupole. This calorimeter will perform a bunch-by-bunch estimate of the luminosity based on the energy deposited in the calorimeter.

The layout of these calorimeters is shown in figure 3.9 and their coverage is summarised in table 3.6. Each of the forward calorimeters will have to deal with high occupancies due

to the presence of background processes, e.g. beamstrahlung, which makes fast readout crucial. Furthermore, the BeamCal experiences a large flux of low energy electrons due to its proximity to the beam pipe, which results in a large radiation dose. This makes radiation hard sensors essential for the BeamCal.

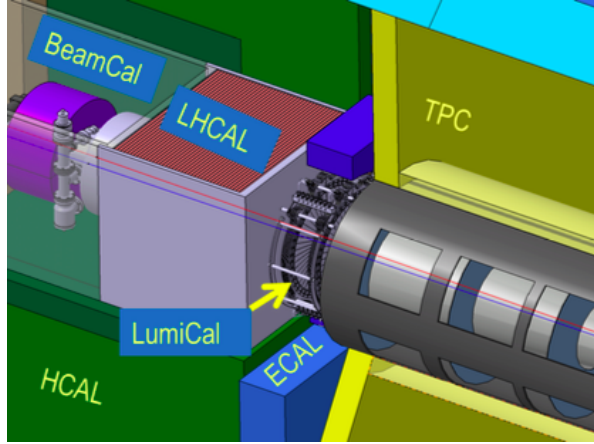


Figure 3.9: The very forward region of the ILD detector. LumiCal, BeamCal and LHCAL are carried by the support tube for the final focusing quadrupole, QD0, and the beam pipe. Figure taken from [26].

| Forward Calorimeter | Polar Angle Coverage [mrad] |
|---------------------|-----------------------------|
| LumiCal | 31 – 77 |
| LHCAL | ~ 29 – 122 |
| BeamCal | 5 – 40 |

Table 3.6: Coverage of the forward calorimeters in the ILD detector.

Each of these forward calorimeters is constructed using tungsten as the absorber material. The small Moli  re radius of tungsten ensures that narrow electromagnetic showers are formed within them, which makes separation and identification of showering particles easier.

The layout of these calorimeters is as follows:

- The LumiCal is a silicon tungsten sampling calorimeter that contains 30 readout layers. This gives the LumiCal a total depth of $\approx 24X_0$.
- The LHCAL is also a silicon tungsten sampling calorimeter, which contains 40 readout layers. The total depth of the LHCAL is $\approx 4\lambda_I$.

- The BeamCal is a tungsten based sampling calorimeter. The sensitive detector material for the BeamCal is an ongoing area of research as, due to the extremely high occupancy from the beam induced backgrounds, a very fast readout is required. The exact layer configuration of the BeamCal will depend upon the choice of sensitive detector material and hence is yet to be specified.

The segmentation within the layers, the cell size, in these forward calorimeter is yet to be fully optimised.

3.3 Simulation

Detector model simulation for all studies presented in this work was performed using MOKKA [36], a GEANT4 [37] wrapper providing detailed geometric descriptions of detector concepts for the linear collider. The MOKKA simulation of the ILD detector contains the following [26]:

- The vertex detector is simulated using silicon as the sensitive material. Support material and the cryostat are also included.
- The supplementary silicon tracking systems are included. Again, material has been added to the simulation to represent the support material for these systems. Furthermore, an estimation has been made of the material budget for power and readout cables from the vertex detector, SIT and FTD and material has been added to the simulation to represent these. The material added to represent the power and readout cables comes in the form of an aluminium cylinder running inside the TPC field cage and around a cone around the beam pipe.
- The TPC is simulated as a cylindrical volume of a gas mixture surrounded by a field cage. A conservative estimate of the endplate is included in the simulation to account for the support structure, electronics and cooling pipes for the TPC.
- As well as including the silicon tungsten sampling calorimeter, the simulation of the ILD ECal contains additional material to represent the instrumented region of the sensor and a heat shield as shown in figure 3.7.
- Simulation of the ILD HCal has a number of realistic features including detailed modelling of the electronics, detector gaps and the implementation of Birk’s law [38] for the scintillator sensitive detector elements.

- The muon system, which is the instrumentation of the iron yoke, uses scintillator as the active material in the simulation. A square cell size of side length 30 mm is assumed. This is in contrast to the nominal ILD model, but as the tail-catcher plays a minimal role in event reconstruction at ILC like energies this difference should have negligible impact.
- The forward calorimeters, the LumiCal, LHCAL and BeamCal, are all included in the simulation. Tungsten is used as the absorber material for each of the calorimeters. The LumiCal and LHCAL use a silicon readout material, while the BeamCal uses a diamond readout.

3.4 CLIC ILD

The increased collision energy of the proposed CLIC accelerator means the use of the nominal ILD detector model would be inappropriate. Therefore, a new detector model, CLIC_ILD [4], based upon the nominal ILD detector model was created to cope with the experimental conditions found at the CLIC experiment. The main differences between the nominal ILD detector and CLIC_ILD are:

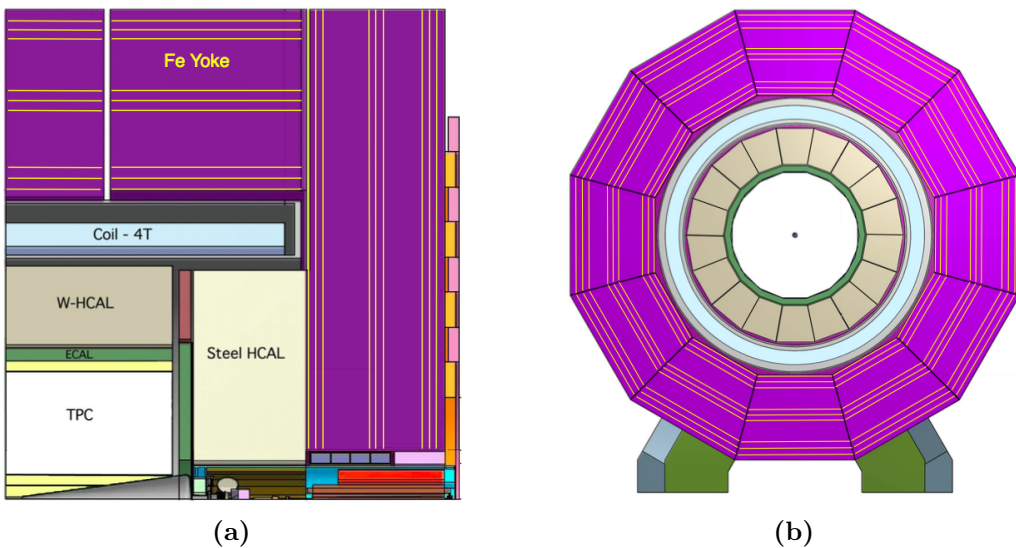


Figure 3.10: (a) Longitudinal (top quadrant) and (b) transverse cross section of the CLIC_ILD detector. Figures taken from [4].

- The higher energies found at the CLIC experiment lead to more intense beam induced backgrounds, which is especially problematic for detectors close to the IP

where the occupancies will be extremely high. For this reason the inner vertex detector in CLIC_{_ILD} is moved 15 mm further out from the IP.

- The HCal thickness is increased from $6 \lambda_I$ to $7.5 \lambda_I$. This ensures that higher energy hadronic showers found at the CLIC experiment are contained within the calorimeters.
- The HCal absorber material for the barrel is tungsten as opposed to steel. This reduces the overall thickness of the HCal and keeps the coil size, one of the driving cost factors for the detectors, similar for the nominal ILD and CLIC_{_ILD} detectors. Steel is used as the absorber material for the HCal endcaps as there are no spatial requirements relating to the coil size and this will lower the detector cost. Furthermore, the shower development time in steel is faster than in tungsten making effective time stamping of energy deposits easier, which is crucial for the CLIC experiment for vetoing beam induced backgrounds.
- The magnetic field strength in the CLIC_{_ILD} detector is increased to 4 T. This was found to benefit the reconstruction, particularly at high energies, as it leads to greater separation of charged particle tracks. Furthermore, it was possible to achieve this increase in field strength using the nominal ILD coil design.
- The CLIC_{_ILD} detector contains masking, graphite layers placed in front of the BeamCal, to prevent particles produced by the beam-induced interactions from backscattering into the main detector. It is the increased collision energy that makes backscattering of particles a more problematic effect for the CLIC experiment than it is for the ILC experiment.

3.5 Particle Flow Reconstruction

Particle flow calorimetry relies upon correct associations being made between calorimetric energy deposits and charged particle tracks. Even with a finely segmented detector, such as the ILD detector described in section 3.2, correctly making these associations is a highly non-trivial task and must be done using advanced pattern recognition software. This is provided by the PandoraPFA particle flow algorithm [24, 25]. PandoraPFA is applied in the linear collider reconstruction using MARLIN [39], a c++ framework specifically designed for the linear collider.

3.5.1 PandoraPFA

PandoraPFA takes as input calorimeter hits and charged particles tracks and produces as output reconstructed particles known as particle flow objects (PFOs). The pattern recognition in PandoraPFA is applied in eight main stages [24]:

1. Track selection. The input track collections are examined to determine whether V^0 decays, two charged tracks originating from a point displaced from the IP, or kinks, where a charged particle has decayed into a single charged particle and a number of neutral ones, are present. Such information will be propagated in the reconstruction to the final PFO creation stage.
2. Calorimeter hit treatment. The treatment of calorimeter hits by PandoraPFA is of paramount importance to the work presented in chapters ?? and ???. Therefore, full details of the calorimeter hit selection procedure are presented here. This selection procedure is broken down into several steps:
 - The various collection of, post digitisation, calorimeter hits are passed into the Pandora framework and converted into Pandora calorimeter hits.
 - To minimise any dependency on the detector geometry each calorimeter hit is assigned to a pseudo-layer, which is representative of the hits position in the calorimeter. All further topological association algorithms work using the pseudo-layer definition, illustrated in figure 3.11.
 - A minimum ionising particle equivalent energy cut is applied to the calorimeter hits. If a calorimeter hit contains less than 0.5 (0.3) of the energy of a normally incident MIP passing through the calorimeter cell in the ECal (HCal) then it is not used in the reconstruction.
 - If a calorimeter hit is sufficiently far away from other hits, it is flagged as an isolated hit. Such hits are most likely due to low energy neutrons produced in hadronic showers, which can travel a significant distance from the original shower before depositing energy. Due to the distance they travel these hits are very difficult to associate to the correct particle shower. Furthermore, as such hits are unlikely to be the seed for a particle shower they are not used by the initial clustering algorithm.
 - Any calorimeter hit that contains an energy consistent with a MIP signal and where, at most, one Pandora calorimeter hit exists in the neighbouring cells

within the same layer is flagged as a MIP consistent hit. This information is used in the identification of MIPs in the reconstruction.

- The energy contribution for each calorimeter hits ultimately depends on whether the cluster the calorimeter hit has been associated to is deemed to have originated from an electromagnetic or hadronic particle shower. Different scale factors are applied to the energy for electromagnetic and hadronic showers to account for the non-compensating response of the calorimeters. These scale factors are used throughout the reconstruction, including the final reconstructed particle energy, once the particle shower type has been identified. For energy comparisons prior to the shower type being identified the uncorrected calorimeter hit energy is used. Further details on how these calibration constants are determined can be found in chapter ??.
3. Clustering. This begins by using the projection of the charged particle tracks onto the front face of the ECal as seeds for the initial clustering phase. Calorimeter hits are looped over on a per layer basis, working from the inner to the outer pseudo-layer, and if they fall within a cone of fixed dimensions surrounding a cluster direction they are associated to the cluster. If no association can be made to any preexisting calorimeter hit clusters then the calorimeter hit is used to seed a new cluster.
 4. Topological cluster merging. The initial clustering algorithm is designed to be conservative to avoid mixing together energy deposits from several particles. The fragments produced by the initial clustering are then merged together by various algorithms whose logic is motivated by a number of well-motivated topological rules, such as those shown figure 3.12.
 5. Statistical re-clustering. Comparisons between the cluster energy and any associated track momenta are made to determine whether they are consistent. If a large discrepancy is observed then statistical re-clustering is initiated. This involves running a number of differently configured algorithms to change the cluster configuration to determine if a new optimal configuration of tracks and clusters can be found.

This step relies upon the reported cluster energies being accurate. To ensure this is the case, a well defined calibration procedure is applied for all detector models considered in this work, for more details see chapter ?. At this point in the reconstruction, the energy resolution of the calorimeters impacts the way that the pattern recognition is performed. The better the energy resolution of the

calorimeters, the fewer the number of mistakes that are made when pairing up clusters of calorimeter hits to charged particle tracks.

6. Photon identification and recovery. Topological likelihood data is used to identify clusters of calorimeter hits that are consistent with γ s. This is possible due to the clear transverse and longitudinal profiles observed for electromagnetic showers.
7. Fragment removal. Neutral clusters originating from a nearby charged particle cluster are identified and merged back into the parent charged particle cluster. These algorithms take into account the changes in the compatibility of the track and cluster associations when merging any neutral clusters into charged clusters.
8. Formation of particle flow objects. Finally, reconstructed particles are produced. The energy for charged particles is taken from the track momenta, while neutral particle energies are taken from the calorimeter cluster measurements. Furthermore, the different electromagnetic and hadronic scales are applied to the output neutral particle energies depending on whether the neutral cluster is consistent with a γ .

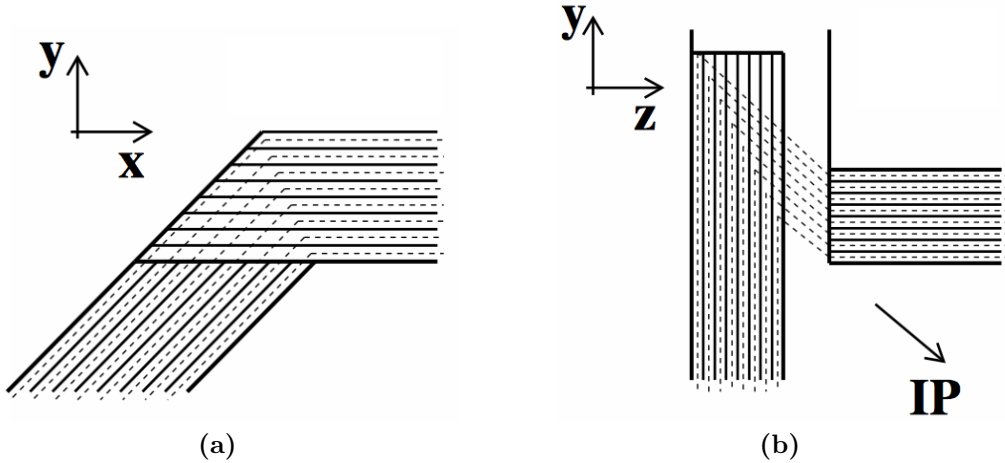


Figure 3.11: Schematic showing the definition of the pseudo-layer assignment for calorimeter hits. The solid lines indicate the positions of the physics ECal layers and the dashed lines show the definition of the virtual pseudo-layers. (a) The xy -view showing the ILD ECal stave structure. (b) The xz view showing a possible layout for the ECal barrel/endcap overlap region. The pseudo-layers are defined using projection back to the IP. Figures taken from [24].

The application of the pattern recognition algorithms in PandoraPFA when combined with a highly segmented detector make particle flow calorimetry a reality. In turn this provides excellent jet energy resolution for studying many interesting physics processes at the linear collider experiment.

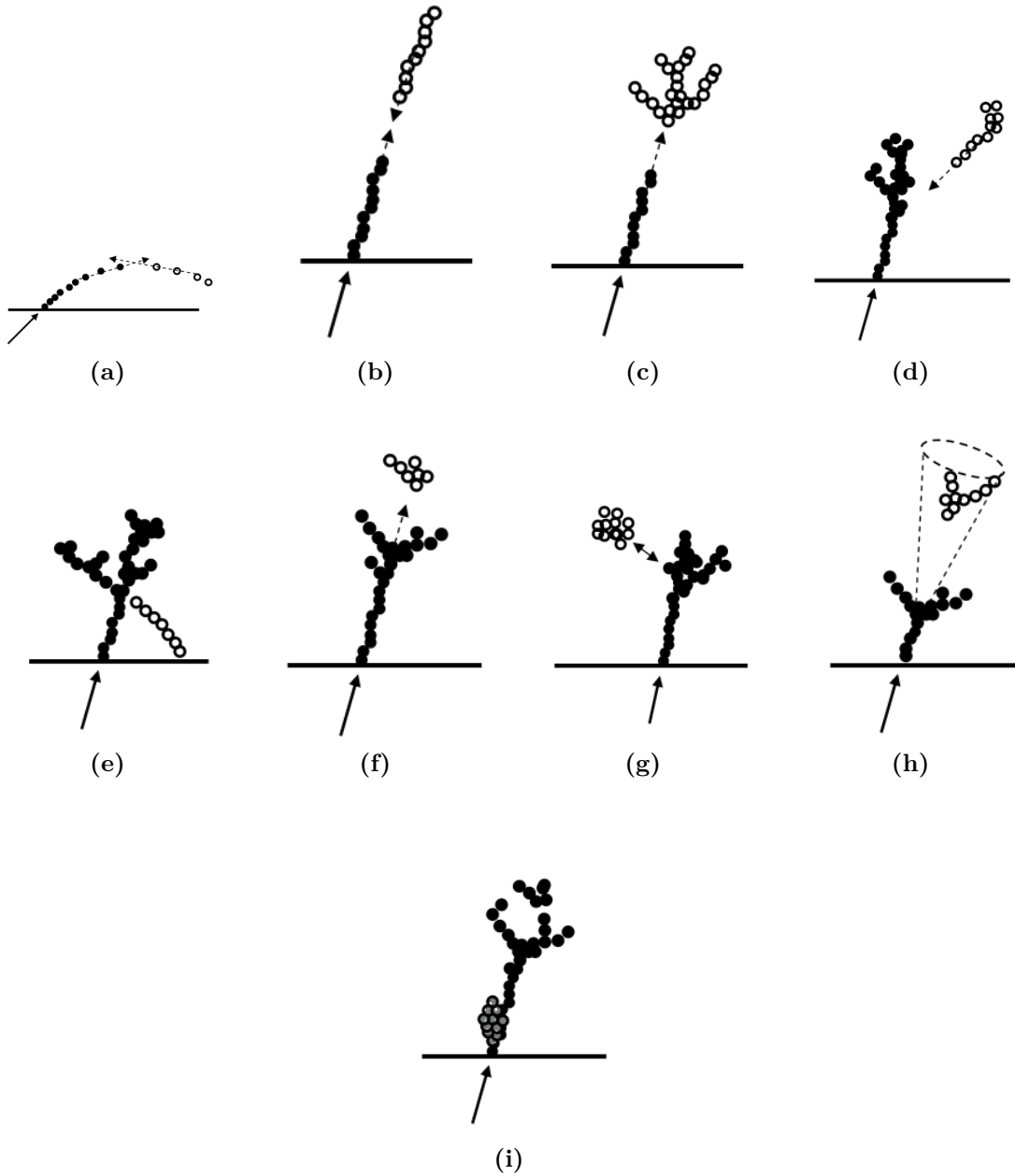


Figure 3.12: The main topological rules for cluster merging: (a) looping track segments; (b) track segments with gaps; (c) track segments pointing to hadronic showers; (d) track-like neutral clusters pointing back to a hadronic shower; (e) back-scattered tracks from hadronic showers; (f) neutral clusters which are close to a charged cluster; (g) a neutral cluster near a charged cluster; (h) cone association; and (i) recover of photons which overlap with a track segment. In each case the arrow indicates the track, the filled points represent the hits in the associated cluster and the open points represent hits in the neutral cluster. Figures taken from [24].

3.6 Performance

The fundamental principle of particle flow calorimetry is to measure the energy of a particle passing through a detector in whichever sub-detector offers the best energy resolution. For particle collider experiments, this involves measuring the momenta of charged particles using the curvature of the track they create in the detector. This offers extremely good energy resolution in comparison to the traditional calorimetric approach.

As many physics processes of interest at the linear collider involve multi-jet final states [40], good jet energy resolution is a crucial aspect of detector performance. As shown in chapter ??, the sensitivity of the linear collider experiment to areas of new physics can be determined using reconstructed jet energies. Furthermore, parameters derived from the energy measurements of jets are extremely useful for identification of physics channels of interest. Therefore, a key metric for describing detector performance is the jet energy resolution. Jet energy resolution in particular can benefit from the application of particle flow calorimetry as $\approx 70\%$ of the energy of jets are carried in the form of charged particles. As particle flow aims to measure the energy of charged particles using the tracker, it has the potential to offer extremely large benefits when measuring jet energies in comparison to the traditional calorimetric approach.

3.6.1 Jet Energy Resolution

The jet energy resolution in these studies was determined through the simulation of off mass shell Z boson events decaying to light quarks (u, d, s). PYTHIA version 6.4 [41], which had been trained on fragmentation data from the OPAL experiment [42], was used to generate these events. The decay of tau leptons appearing in the day was simulated using TAUOLA [43]. Detector simulation and event reconstruction was carried out as described in sections 3.3 and 3.5 respectively.

As the Z boson in these events is produced at rest, the typical decays form two mono-energetic jets that are produced back-to-back as shown in figure 3.13. Only events where $|\cos(\theta)| < 0.7$, where θ is the polar angle of the quarks, are used in the jet energy resolution calculation. This ensures little energy is lost down the beam axis. Using these events, the jet energy resolution was calculated as follows:

$$\frac{\text{RMS}_{90}(E_j)}{\text{Mean}_{90}(E_j)} = \frac{\text{RMS}_{90}(E_{jj})}{\text{Mean}_{90}(E_{jj})} \times \sqrt{2}, \quad (3.2)$$

where E_{jj} is the total reconstructed energy. The variables $\text{Mean}_{90}(E_{jj})$ and $\text{RMS}_{90}(E_{jj})$ are the mean and root mean squared (RMS) of the E_{jj} distribution respectively. They are calculated across the range of E_{jj} with the smallest RMS containing at least 90% of the data. This definition is used to remove the effect of outliers in the distribution [24]. If all associations between charged particle tracks and calorimeter clusters were correctly made, the reconstructed jet energy distribution would be Gaussian. However, the effect of confusion on certain events will distort this distribution and broaden the tails significantly. If the full range were to be used in the jet energy resolution calculation, the effect of these tails is overinflated. If the distribution of reconstructed jet energies is truncated to the narrowest range of the data containing at least 90% of the data, the effect of these tails can be negated. This removes events where confusion is dominant, which makes the jet energy resolution metric far more robust and representative of the bulk of the data.

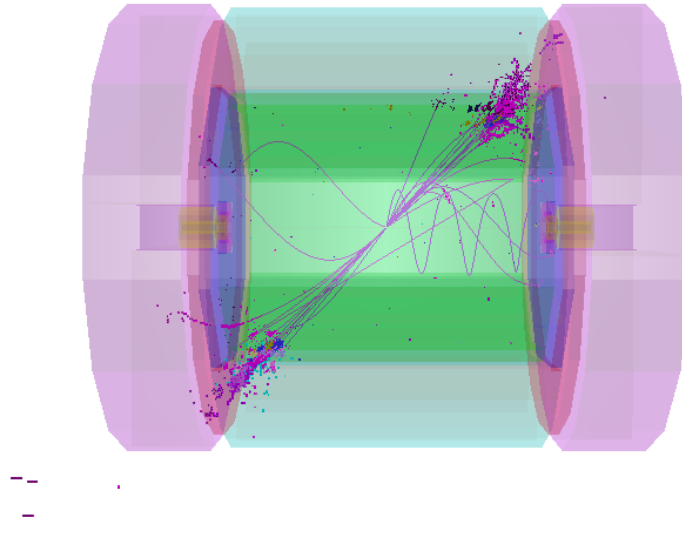


Figure 3.13: 500 GeV di-jet $Z \rightarrow u\bar{d}s$ event display for nominal ILD detector.

An example of the application of this metric can be found in figure 3.14. In this example $\text{RMS}(E_j)$, the RMS calculated using the full range, is 5.8 GeV, while $\text{RMS}_{90}(E_j)$, the RMS using the reduced range, is 4.1 GeV. This corresponds to a reduction in the jet energy resolution from 4.1% to 2.9%, which clearly shows an overemphasis of the tails of the distribution when using the full jet energy range.

In the subsequent analysis a range of di-jet energies were considered ranging from the Z mass, 91 GeV, to the nominal running energy of the ILC, 500 GeV. Each event

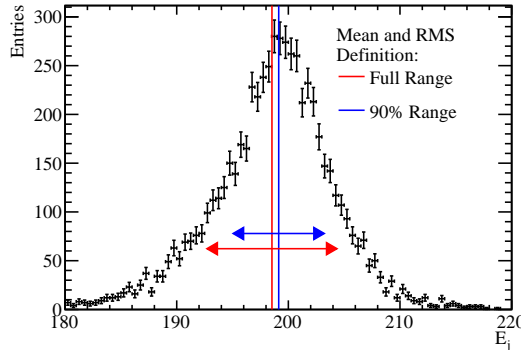


Figure 3.14: Definition of jet energy resolution. Reconstructed jet energy for 200 GeV di-jet $Z \rightarrow u\bar{d}s$ events for nominal ILD detector. The solid vertical line shows the mean of the distribution and the horizontal arrows indicate the mean \pm the root mean square (RMS) of the distribution. The red and blue lines show the mean and RMS calculated using the full range and 90% of the full range with the smallest RMS respectively.

sample contained 10,000 events generated isotropically so that, given the polar angle cut, approximately 7,000 events contribute to the jet energy resolution calculation.

3.6.2 Decomposition of the Jet Energy Resolution

It is possible to gain additional insight into the detector performance by cheating the pattern recognition, the clustering of calorimeter hits together and the creation of track to cluster associations, using MC information. Cheating the pattern recognition removes the effect of confusion as it ensures no errors are made when either clustering calorimeter hits together or when associating charged particle tracks to those calorimeter clusters. This allows the detector performance to be deconstructed into two terms; one related exclusively to the intrinsic energy resolution of the detector and another related to the pattern recognition confusion. The additional information this provides is extremely useful for characterising changes to the overall detector performance.

The intrinsic energy resolution contribution to the jet energy resolution is determined by fully cheating the pattern recognition; in this case all confusion is negated. The total confusion is defined as the quadrature difference between the jet energy resolution using the standard reconstruction and this fully cheated reconstruction. Furthermore, it is possible to cheat the pattern recognition associated with individual types of particles. This is particularly useful for studies related to the ECal as, by cheating the photon

pattern recognition, it is possible to isolate the confusion associated with photons. The photon confusion is defined as the quadrature difference between the jet energy resolution using the standard reconstruction and the reconstruction where the photon pattern recognition is cheated. Examples of the calculation of the various confusion terms defined above are given in table 3.7.

| Reconstruction | Jet Energy Resolution [%] |
|---|------------------------------------|
| Standard Reconstruction (No MC Information) | $a = 2.97 \pm 0.05$ |
| Cheating Entire Reconstruction | $b = 1.69 \pm 0.02$ |
| Confusion | $\sqrt{a^2 - b^2} = 2.45 \pm 0.05$ |
| Cheating Photon Reconstruction | $c = 2.73 \pm 0.04$ |
| Photon Confusion | $\sqrt{a^2 - c^2} = 1.18 \pm 0.06$ |

Table 3.7: Example calculation of the confusion contributions to the jet energy resolution. These jet energy resolutions are for 250 GeV jets using the nominal ILD detector model and are calculated using the range of jet energies with the smallest RMS containing at least 90% of the data.

A common feature that is observed in these calibration studies is that as the intrinsic energy resolution of a calorimeter improves, the effect of confusion is reduced. This occurs as a better energy resolution means more precise comparisons can be made between the energy of a cluster of calorimeter hits and the momentum of any charged particle tracks associated to it. Comparisons such as these are made by PandoraPFA to determine whether the track cluster associations that have been made are consistent. If a large discrepancy is observed between the cluster energy and track momenta, the clustering of calorimeter hits is modified until a consistent association can be made. For more details on this comparison see chapter 3. This consistency check vastly reduces the number of errors made when clustering calorimeter hits and associating charged particle tracks to those clusters i.e. the confusion. Therefore, improving the precision of this consistency check, by improving the energy resolution, reduces the effect of confusion.

3.6.3 Single Particle Energy Resolution

The energy resolution for individual particles is crucial for a number of physics studies of interest to the linear collider, such as γ energy resolutions in the study of anomalous triple and quartic gauge couplings [44–46]. Therefore, γ and K_L^0 energy resolutions, alongside

the jet energy resolution, will be considered in these optimisation studies. As both γ and K_L^0 are uncharged, their energy measurements will be made using the calorimeters as opposed to the tracker. γ s are a natural choice of particle to consider as they are particularly relevant for several physics studies and, as they are largely contained within the ECal, they will be highly sensitive to changes in the ECal performance. K_L^0 s were used as, analogously to γ s and the ECal, their energies are primarily measured using the HCal. In general, neutral hadron energy resolutions are less crucial to physics studies, however, they do make crucial contribution to the jet energy resolution that should not be overlooked. The reported γ energy resolutions were determined using events containing a single 100 GeV γ , while the K_L^0 energy resolutions were determined using events containing a single 50 GeV K_L^0 . These energies were chosen to be as large as possible, to maximise sampling of the calorimeter response, while minimising the affect of leakage of energy from the ECal to the HCal for the γ events and leakage of energy out of the rear of the HCal for the K_L^0 events.

The energy resolution for these single particle samples is determined using a Gaussian fit to the reconstructed energy distributions. To aid convergence, the fit was applied to the narrowest range of the reconstructed energy distribution containing at least 75% of the data. The single particle energy resolution is defined as the standard deviation divided by the mean of the fitted Gaussian. For each energy resolution calculation, a total of 10,000 events were used to populate the reconstructed energy distribution. For clarity, a cut of $|\cos(\theta)| < 0.7$ was applied to veto events where particles travelled down the beam pipe or where they passed through the barrel/endcap overlap region. An example of the reconstructed energy distributions for 100 GeV γ s and 50 GeV K_L^0 s, alongside the Gaussian fits used to determine the energy resolutions, are shown in figure 3.15. The errors quoted on single particle energy resolutions are determined by propagating the errors reported from the Gaussian fit into the resolution calculation.

3.7 Summary of ILD Detector Performance

The following section outlines the nominal ILD detector performance using the metrics outlined in section 3.6.

The reconstructed energy distributions for particles whose energies are measured using calorimeters will be Gaussian. This is the case for sampling calorimeters as the active material in each calorimeter hit essentially counts the number of charged particle

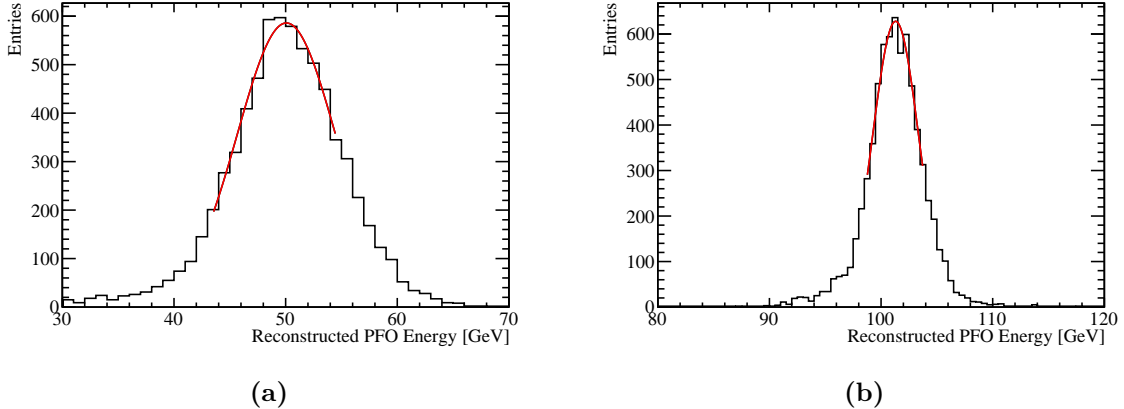


Figure 3.15: The reconstructed energy distribution for (a) 50 GeV K_L^0 and (b) 100 GeV γ events. The red line shows a Gaussian fit used to parameterise the detector performance. The fit was applied to the truncated range of the reconstructed PFO energy distribution containing at least 75% of the data with the narrowest RMS. The nominal ILD model was used in this simulation.

tracks passing through it, or possible the number of photons for scintillator options. An estimation of the total energy deposited in a calorimeter hit, including the absorber material, can be made based upon this number of tracks or photons. For more details on how this estimation is made see chapter ???. Finally, the energy of the entire particle shower is estimated by grouping together calorimeter hits and summing their energy. As each calorimeter hit energy is an independent random measurement the particle shower energy will, by the central limit theorem, have a Gaussian distribution.

As each calorimeter hit involves counting a number of objects, charged particle tracks or photons, Poisson statistics governing the distribution of calorimeter hit energies. If the mean of the distribution of the energy of a cluster of calorimeter hits is $\lambda = N$, where N is the mean number of objects the are measured in the calorimeters, the standard deviation of that distribution is $\sigma = \sqrt{\lambda} = \sqrt{N}$ and the energy resolution is $\frac{\sigma}{\lambda} = \frac{1}{\sqrt{N}}$. As the total shower energy, E_{Reco} , is proportional to N the energy resolution for a particle shower in an ideal calorimeter is $\frac{\sigma_{Reco}}{E_{Reco}} = \frac{a}{\sqrt{E_{Reco}}}$. In reality, it is typical to express the energy resolution of a calorimeter in the following form

$$\frac{\sigma_{Reco}}{E_{Reco}} = \frac{a}{\sqrt{E_{Reco}}} \oplus b \oplus \frac{c}{E_{Reco}}, \quad (3.3)$$

where the b term is a constant term that accounts for a variety of instrumental effects that do not depend on energy, e.g. mechanical imperfections, and the c term accounts for electrical noise [47]. Here \oplus denotes the quadrature sum of variables.

Prototypes of the various ILD calorimeter options have been constructed and validated using test beam measurements. The energy resolution of the ILD ECal, determined from test beam measurements, was parameterised as $\frac{16.6}{\sqrt{E_{Reco}}} \oplus 1.1\%$ for the silicon option and $\frac{12.9}{\sqrt{E_{Reco}}} \oplus 1.2\%$ for the scintillator option [26]. The electrical noise was deemed sufficiently small that the c term in the parameterisation could be neglected in both cases. These results were determined using an e^- test beam with energies ranging up to ≈ 40 GeV. This parametrisation is compared to the full ILD detector simulation in figures 3.16a and 3.16b for the silicon and scintillator ECal options respectively. The test beam parameterisation of the energy resolution for the silicon ECal option is almost identical to the energy resolution observed in the full simulation. At very high energies, ≈ 500 GeV, the ECal is no longer sufficient to fully contain the γ s and so leakage of energy into the HCal leads to a minor degradation in the simulated energy resolution. This accounts for the worse energy resolution seen in the full simulation when compared to an extrapolation of the test beam parameterisation at high energies. The test beam parameterisation of the energy resolution for the scintillator ECal option is significantly better than that observed in the full simulation, which is most likely due to an imperfect implementation of the scintillator ECal within the full detector simulation. The γ energy resolutions seen in the full ILD simulation are similar for the silicon and scintillator ECal options.

Similarly, the energy resolution, determined from test beam measurements, for the nominal ILD HCal was parameterised as $\frac{57.6}{\sqrt{E_{Reco}}} \oplus 1.6\%$ [48]. A comparison between this test beam parameterisation and the full ILD simulation, using the silicon ECal option, is shown in figure 3.16c. The test beam measurements were made using π^\pm s with energies ranging from 10 to 80 GeV, while the full ILD simulation used K_L^0 s ranging from 10 to 100 GeV. The deviation between the test beam parameterisation and the full ILD simulation, which grows as the K_L^0 energy increases, is most likely due to the treatment of energy deposits leaking out of the back of the HCal. In the test beam studies, to minimise the effect of leakage, events were only considered if the particle showers started developing at the front of the HCal. In the full simulation studies, all particle showers were used, which means some energy will have leaked out of the back of the calorimeters and been deposited in the uninstrumented solenoid region of the detector resulting in a degradation in the energy resolution.

Figure 3.16d shows the jet energy resolution as a function of jet energy for the full ILD simulation. Alongside this, the intrinsic energy resolution and confusion contributions to the jet energy resolution are also presented. The jet energy resolution at low energies is dominated by the intrinsic energy resolution of the detector, while at high energies it is dominated by the effect of confusion. This is to be expected because the intrinsic energy resolution of the calorimeters is proportional $\frac{1}{\sqrt{E_j}}$. On the other hand, confusion grows with energy because increasing energy leads to more dense event topologies, which makes pattern recognition more challenging. The total jet energy resolution for the ILD detector are sufficiently small, $\frac{\sigma_{E_j}}{E_j} \lesssim 3.8\%$ [4, 24, 26], across the energy range considered to make separation of the hadronic decays of the W and Z bosons possible, which is one of the key requirements for the future linear collider.

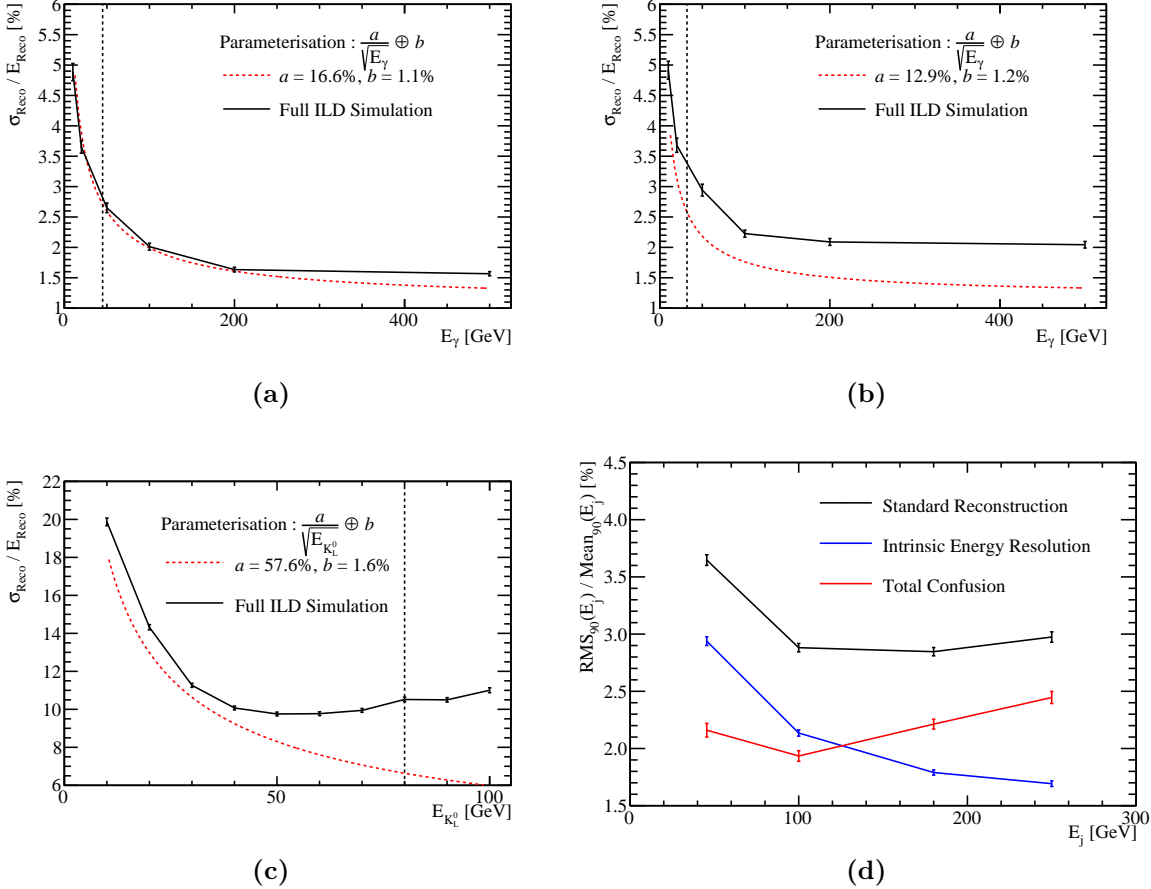


Figure 3.16: (a) The energy resolution as a function of γ energy for the silicon ECal option. The black markers indicate the energy resolutions for the full ILD simulation and the red dotted line shows the test beam parameterisation of the ECal energy resolution. (b) The energy resolution as a function of γ energy for the scintillator ECal option. The black markers indicate the energy resolutions for the full ILD simulation and the red dotted line shows the test beam parameterisation of the ECal energy resolution. (c) The energy resolution as a function of neutral hadron energy. The black markers indicate the energy resolutions for the full ILD simulation, with the silicon ECal option, which was determined using K_L^0 s. The red dotted line shows the test beam parameterisation of the HCal energy resolution, which was determined using π^\pm s. (d) The jet energy resolution (RMS_{90}) as a function of jet energy using the nominal ILD model, with the silicon ECal option. The intrinsic energy resolution and confusion contributions these the jet energy resolutions are also presented. The black dotted vertical line on the single particle energy resolutions shows the highest energy particles used in the test beam measurements.

Chapter 4

Capacitively Coupled Pixel Detectors for the CLIC Vertex Detector

“There, sir! that is the perfection of vessels!”

— Jules Verne, 1828–1905

4.1 Introduction

Identification of heavy-flavour quarks and tau-leptons at any of the currently proposed linear collider experiments will rely upon precise reconstruction of secondary displaced vertices that are produced when these particles decay. Furthermore, the ability to accurately associate any daughter tracks produced in such decays to the secondary vertices is essential. At CLIC, this can only be realised using a vertex detector with a very high spatial resolution, of approximately 3 μm , and good geometric coverage, extending to low polar angles θ . The vertex detector must also have a low material budget (less than 0.2 % X_0 per layer) in order to prevent additional decay vertices from material interactions, and allow efficient track reconstruction despite the high presence of beam-induced background particles. Tracking in the vertex detector will be aided by the use of time-stamping of individual hits, to an accuracy of 10 ns, to identify particles produced from the physics event of interest.

As there are currently no technology options that fulfil all of the criteria for the CLIC vertex detector, the CLIC experiment has developed an extensive R&D program where new technologies for the vertex detector are considered. High-voltage complementary metal-oxide-semiconductor (HV-CMOS) sensors, which are capacitively coupled to a separate readout application-specific integrated circuit (ASIC) are one such option. The performance of prototype detectors based upon this technology and the impact of mechanical tolerances present in their manufacture are presented in this chapter.

4.1.1 HV-CMOS

Pixel detectors can be broadly classified in two groups: hybrid detectors, where a separate sensor and readout chip are bonded together; and fully-integrated devices, where the collection diode is implanted in the same piece of silicon as the readout circuitry. Fully-integrated devices have traditionally not been suitable for applications with high timing requirements, due to the relatively slow charge collection time and limited on-pixel functionality. However, recent developments in CMOS technologies have led to new detector designs that may overcome some of these issues.

HV-CMOS is a processing technology whereby the n-MOS and p-MOS transistors forming the on-pixel electronics are placed entirely within a deep n-well, as shown in figure 4.1. By varying the voltage applied at the gate terminal, n-MOS and p-MOS transistors are able to control the current flowing between the source and drain terminals. The gate voltage produces an inversion layer between the source and drain terminals that acts as a conduit, allowing current to flow between the source and drain as shown in figure 4.2. The voltage at the gate, with respect to the body, controls the width of the inversion layer and hence the magnitude of this current. Logic operations can be performed directly on-pixel using various configurations of n-MOS and p-MOS transistors.

For the HV-CMOS, the deep n-well housing the on-pixel electronics acts as the charge collection diode as well as shielding the circuitry from the p-substrate. This shielding allows for the application of a moderate bias voltage to the sensor bulk that produces a depletion region, which facilitating fast charge collection via a drift current. In contrast, traditional monolithic active pixel sensors (MAPS) have a much smaller depletion region meaning charge collection occurs primarily through the slower mechanism of diffusion.

Furthermore, in conventional MAPS there is potential for competition for charge collection between the n-well collecting diode and the p-MOS transistors used to perform

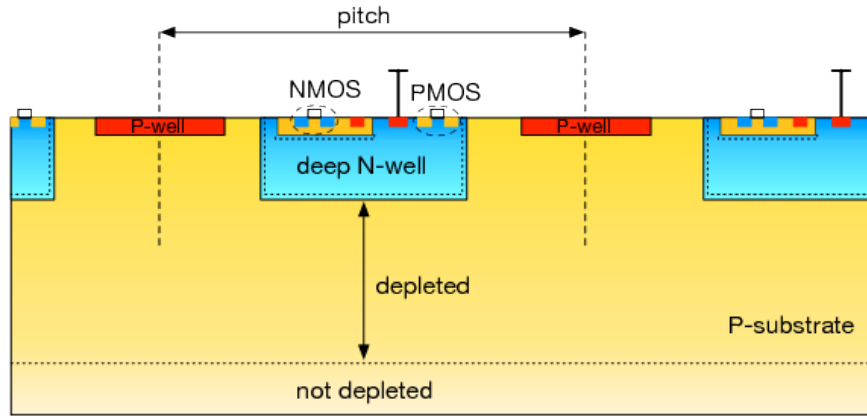


Figure 4.1: Schematic cross section of an HV-CMOS sensor: the deep n-well is the charge-collecting electrode and also contains additional CMOS circuitry such as a preamplifier. Image taken from [49].

μ

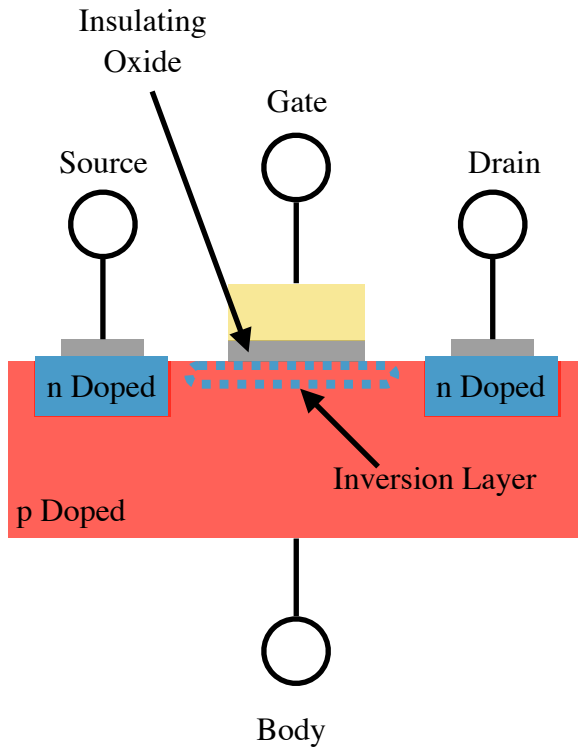


Figure 4.2: Schematic cross section of an n-MOS transistor. p-MOS transistors have a similar cross section where the n and p doped regions are switched.

logic operations as the p-MOS transistors are embedded within an n-well. This only occurs as the n-well collection diode is separated from the n-wells housing the p-MOS transistors. HV-CMOS technology does not suffer from this issue as the deep n-well

collecting diode houses the p-MOS transistors meaning charge is only collected at a single well in the sensor bulk.

HV-CMOS technology thus offers the possibility of fast charge collection with integrated on-pixel functionality, but several limitations still exist. As the on-pixel electronics have to be placed inside the deep n-well and the n-wells of neighbouring pixels have to be isolated from each other, there is a limited physical area of the pixel that can be used for transistor layout, which limits the available on-pixel functionality. In addition to this, it is not possible to implement full CMOS logic inside the deep n-well as coupling between p-MOS transistors and the collection diode will lead to noise injection at the charge collection node. While it is possible to embed p-MOS transistors within a p-well to shield them from the deep n-well, so-called "quadruple-well technology", to give access to full CMOS logic this option is not readily available for prototyping. By restricting the complexity of on-pixel electronics and using a separate readout ASIC, it is possible to overcome many of these issues. When coupled with the fast charge collection time and removal of competition in charge collection this makes HV-CMOS technology highly desirable for use in the CLIC vertex detector.

4.1.2 CLIC ASICs

As HV-CMOS technology is such a promising option for use at the CLIC vertex detector, prototype devices based on this technology have been developed for testing. Two ASICs have been developed: the capacitively coupled pixel detector version 3 (CCPDv3), a sensor chip based on HV-CMOS technology, and the CLICpix, a readout chip providing additional on-pixel logic operations. The pixel pitch of the chips, both the CCPDv3 and the CLICpix, is 25 μm , which should be sufficient to meet the requirements for the CLIC vertex detector. Each of the prototype ASICs consists of a matrix of 64×64 pixels. The CCPDv3 is fabricated in a 180 nm HV-CMOS process, where 180 nm refers to the smallest size building block that can be used for creating the integrated circuits on a silicon wafer. This is comparable to device fabrication at the LHC, which typically uses a 130 and/or 250 nm CMOS processes [50, 51]. In comparison, the CLICpix is fabricated in a 65 nm process, which makes it possible to have more complex on-pixel circuitry incorporated into it than would be possible in previous generations of pixel detectors. A schematic of these devices can be found in figure 4.3.

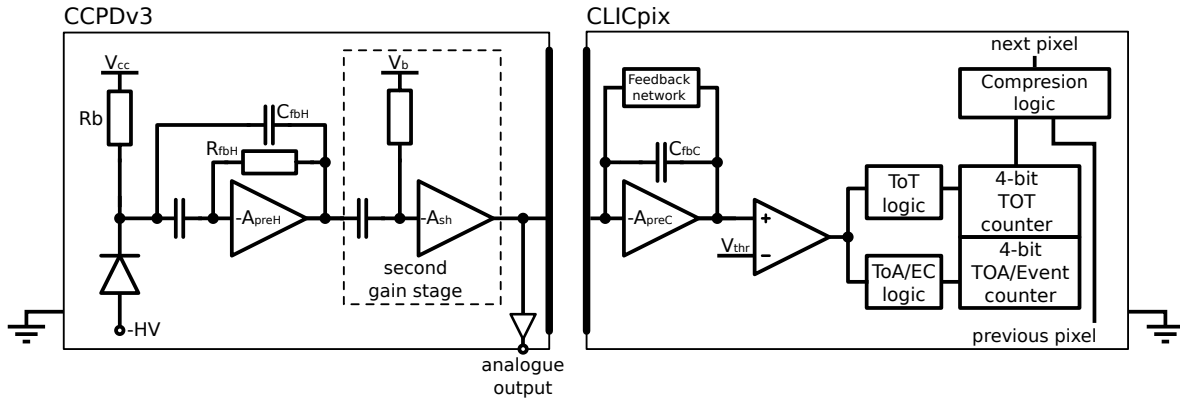


Figure 4.3: Schematic of CCPDv3 and CLICpix pixels.

4.1.2.1 CLICpix

CLICpix is a hybrid pixel readout chip that has been developed for the CLIC vertex detector. Each CLICpix pixel contains a charge-integrating amplifier connected to a discriminator, as shown in figure 4.3. The discriminator remains high for as long as the input signal is over a given threshold, and this output is then used as the input for further logic operations. The additional logic operations record the time of arrival and magnitude of the collected charge, using a Time over Threshold (ToT) measurement. The ToT is stored in a 4-bit on-pixel counter.

The CLICpix operates using a shutter-based readout, where the entire matrix is kept active while the shutter is open and when closed the matrix is readout in its entirety. This is designed to match the expected beam structure for the CLIC experiment, as the accelerator will deliver bunch trains of e^+ and e^- that are separated by 20 ms. Each bunch train contains 312 bunches with a spacing of 0.5 ns, giving a total train length of 156 ns. Furthermore, the shutter-based readout is well suited to power-pulsing, where the power to the front-end electronics is turned off between bunch crossings. This helps to significantly reduce the power consumption of the detector.

The threshold voltage, the voltage required for the discriminator to register an output, seen by each CLICpix pixel is slightly different due to variations in the manufacturing process. If these variations are not accounted for then the behaviour of the device across the matrix will not be uniform. To minimise the impact of these fluctuations, each CLICpix pixel contains a 4-bit local adjustment to the threshold voltage, which is calibrated to unify the response across the matrix. The threshold "equalisation" is achieved by performing two threshold scans across the matrix, once with all four bits

set to 0 (no local threshold adjustment), and a second time with all four bits set to 1 (maximum local threshold adjustment). For each scan, the baseline voltage of each pixel is determined. By applying a linear interpolation between the 0000 and 1111 cases, each pixel can be tuned to a common point, such that all pixels respond at the same global threshold.

4.1.3 Capacitive Coupling

Solder bump-bonding is typically used to connect the sensor and readout ASIC in hybrid pixel detectors. This procedure uses small spheres of solder to connect each pixel on the sensor to the corresponding pixel on the readout ASIC. There are several drawbacks to the use of this procedure for pixel detectors: it is expensive and sets limits on the thickness of both ASICs that is required for mechanical stability. An alternative procedure for connecting the sensor and readout ASICs involves using a thin layer of glue to form a capacitive connection between the two. This procedure reduces the cost and material budget with respect to bump-bonding, making it highly desirable for use in the CLIC vertex detector. In order to make this viable, it is necessary to implement an amplifier in the CCPDv3 pixel, shown in figure 4.3, to boost the signal and overcome the intrinsically small coupling capacitance.

4.2 Device Fabrication

There are two issues related to device manufacture that have to be considered when using capacitive coupling to connect the sensor and readout ASIC: the uniformity of the glue layer and the spatial alignment of the sensor and readout pads. The former has been investigated in [CERN FABRICATION NOTE CITE], while the latter is the focus of this study. In order to characterise the impact on detector performance of any misalignment between the CCPDv3 and the CLICpix pads, a number of assemblies have been constructed that purposefully contain misalignments, as shown in figure 4.4. Table 4.1 contains a summary of the samples produced.

The full details of the glueing procedure can be found in [CERN FABRICATION NOTE CITE], along with a study of the absolute precision of the manufacturing procedure. For devices constructed in an identical fashion to those considered here, the glue layer

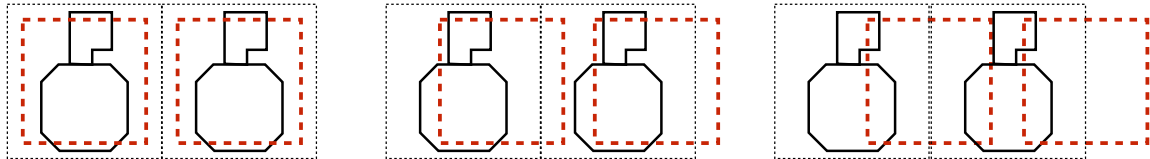


Figure 4.4: Alignment schematic of the CCPDv3 and CLICpix detectors studied. The red dotted line represents the CCPDv3 pad and the solid black line represents the CLICpix top metal layer. From left to right; centred pixels, 1/4 offset ($6.25 \mu\text{m}$) and 1/2 offset ($12.5 \mu\text{m}$).

| Assembly | Alignment |
|----------|----------------------|
| SET 9 | Centred |
| SET 10 | $\frac{1}{4}$ Offset |
| SET 12 | Centred |
| SET 13 | Centred |
| SET 15 | Centred |
| SET 16 | $\frac{1}{2}$ Offset |

Table 4.1: A list detailing the alignment of the CCPDv3 and CLICpix coupling pads for the devices considered in this study.

thicknesses were less than $1 \mu\text{m}$ and the precision on the pad positioning was less than $2 \mu\text{m}$.

4.3 Device Characterisation

A series of laboratory experiments were used to characterise the devices produced for this alignment study. The devices were also tested in realistic experimental conditions using the CERN SPS test beam. Due to the complexities of testing devices in a test beam, extensive laboratory test were performed first to characterise as many properties of the assemblies as possible. The laboratory experiments performed were:

- **Radioactive source measurements.** The goal of this measurement is to measure the response of the CCPDv3 and CLICpix when a radioactive source is used to deposit charge within the CCPDv3 sensor.

- **Test pulse calibration of the CLICpix chip.** The goal of this measurement is to calibrate the response of the CLICpix sensor. This is achieved by examining the CLICpix response when injecting a quantity of charge directly into the input of the chip, which bypasses the CCPDv3 and glue layer.

4.3.1 Source Measurements

A radioactive source was used to deposit charge within the CCPDv3 sensor and the response of the CCPDv3 and CLICpix examined. The CCPDv3 sensor converts the deposited charge into a voltage, which in turn passes through the capacitive glue layer and into the CLICpix chip. Measurements were made of the output voltage produced by the CCPDv3 and the response of the CLICpix readout chip, in units of ToT. As the exact amount of charge deposited by the radioactive source is unknown, calibration of the CCPDv3 is not possible. Instead, this experiment focuses on examining the shape of the voltage produced by the CCPDv3 and determining the response of the CLICpix chip as a function of this voltage. As the CCPDv3 signal passes through the capacitively coupled glue layer before entering the CLICpix chip, this study characterises the properties of the gluing layer as well as the sensor and readout chips.

4.3.1.1 Experimental Setup

The radioactive material used in this study was Sr⁹⁰. Sr⁹⁰ undergoes β^- decay to form Y⁹⁰, which in turn undergoes β^- decay to form the stable isotope Z⁹⁰. Each β^- decay produces an e⁻ and a $\bar{\nu}_e$, and the e⁻ goes on to deposit charge in the CCPDv3 sensor. The Sr⁹⁰ source used had an activity of 29.6 MBq.

The radioactive source was positioned directly above the back-side of the CCPDv3 sensor, and measurements were made of both the ToT output from the CLICpix and the CCPDv3 analogue signal for individual pixels on the sensor. The CCPDv3 pulse shape was recorded on a fast sampling oscilloscope that was also used to trigger the CLICpix readout. The on-pixel event counter, which is located in the CLICpix chip, was used to veto events where multiple hits occurred within the active shutter period. The CCPDv3 sensor was biased to 60 V during this experiment. Examples of CCPDv3 output voltage pulses when using the Sr⁹⁰ source can be seen in figure 4.5. The analogue output has a baseline voltage of ≈ 1.15 V, with signal saturation occurring around a height of 700 mV.

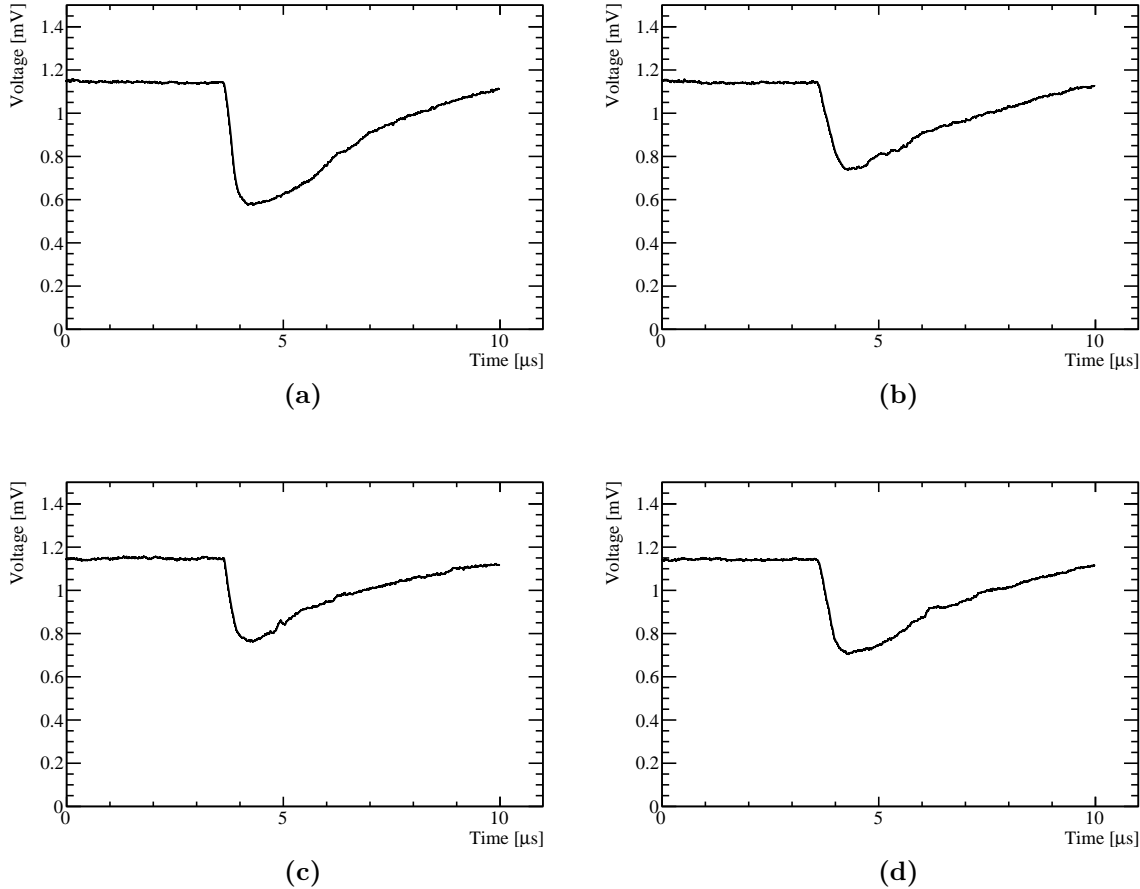


Figure 4.5: CCPDv3 voltage pulses produced using a radioactive source, Sr^{90} , to deposit charge in the sensor.

4.3.1.2 Analysis

The quantities of interest related to the CCPDv3 output voltage are the pulse height, defined as the peak of the voltage pulse, and the rise time, defined as the time it takes for the CCPDv3 to reach the pulse height. For ease of analysis the baseline voltage is subtracted from the CCPDv3 output voltage and the pulse shape inverted before the following analysis is applied to extract the variables of interest.

The pulse height is defined using a Gaussian fit to the peak of the voltage pulse. This method is used to minimise the dependency of the pulse height on small fluctuations in the output voltage. The peak of the voltage pulse is defined as the region where the change in the CCPDv3 voltage output is greater than 90% of the maximum change in the CCPDv3 voltage output.

The rise time is defined as the time taken for the signal to go from 10% to 90% of the maximum change in the CCPDv3 voltage output. This definition makes the rise time metric more robust against fluctuations in the CCPDv3 voltage output.

Examples of the calculation of these metrics for a representative pulse is shown in figure 4.6. Due to the design of the CCPDv3 matrix, it is only possible to record the CCPDv3 voltage output for 15 pixels running along one edge of the 64×64 matrix. Therefore, in the subsequent analysis data was taken for each of these accessible pixels and combined.

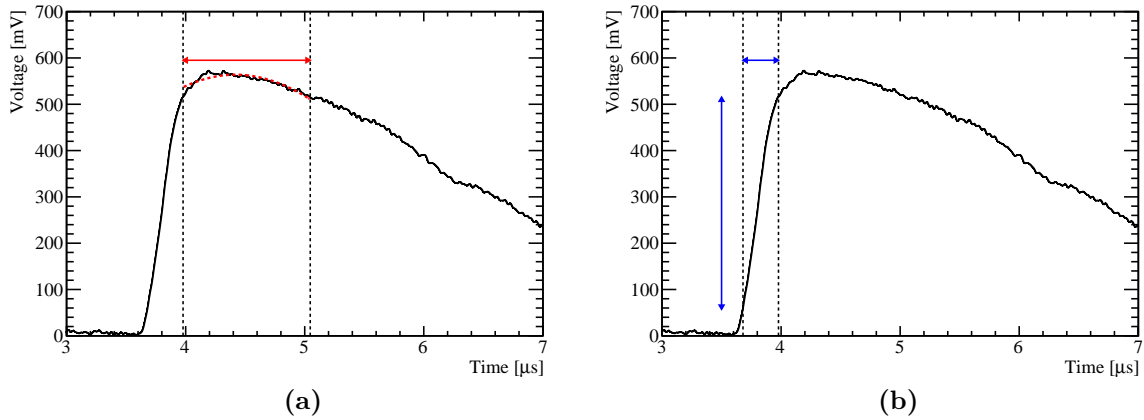


Figure 4.6: An example calculation of the pulse height and rise time for the CCPDv3 output voltage. In this example the black line show the CCPDv3 output voltage as a function of time where the baseline voltage has been subtracted and the pulse shape inverted. These voltage pulses were created using a radioactive source, Sr^{90} , to deposit charge in the sensor. (a) The definition of the pulse height. Pulse height is defined as the amplitude of a Gaussian function fitted across the peak of the voltage pulse. The peak of the voltage pulse is defined as the region where the voltage in excess of 90% of the raw pulse height, which is indicated in the figure by the red arrow. The red dotted line shows the Gaussian fit used to extract the pulse height. (b) The definition of rise time. Rise time is defined as the time taken for the CCPDv3 voltage to rise from 10% to 90% of the raw pulse height. The rise time, and change in CCPDv3 output voltage over this time, are shown in the figure by the blue arrows.

4.3.1.3 Results: Rise Time vs Pulse Height

The mean rise time as function of pulse height for the CCPDv3 output voltage is shown in figure 4.7. This was determined by binning the measurements in pulse height and determining the mean rise time for measurements in each bin. The pulse height

was binned using a bin width of 4 mV ranging from 0 to 700 mV. A minimum of 10 measurements per bin were used for the calculation of the average rise time. The error bars on this figure show the standard error in the mean rise time. Data was only included in this analysis if the on-pixel event counter registered a single hit in the time window used to take data.

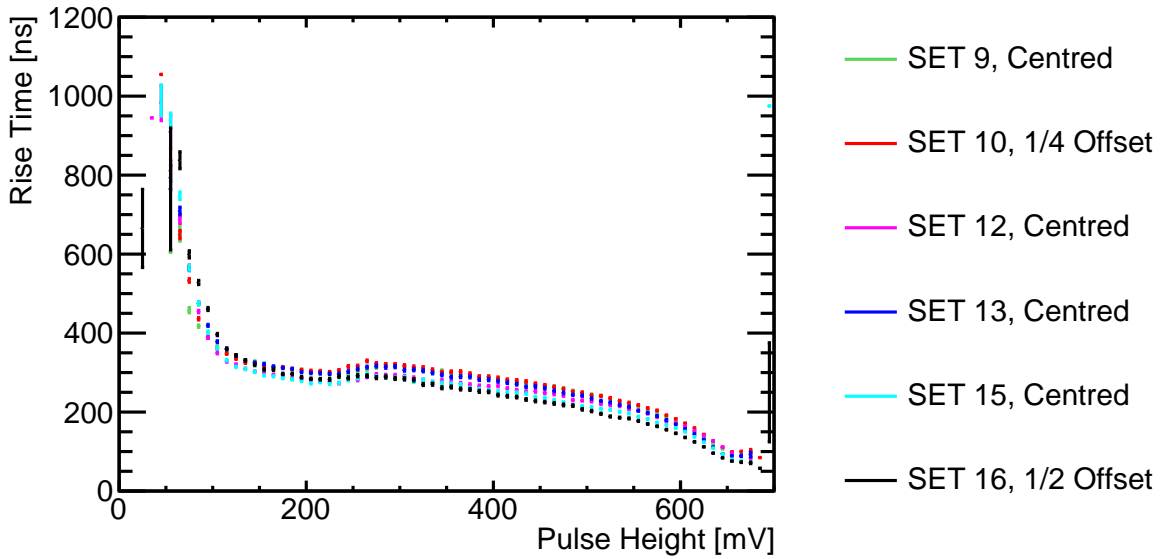


Figure 4.7: The CCPDv3 output voltage rise time as a function of pulse height.

The data in figure 4.7 shows that the rise time for the CCPDv3 front-end is approximately 300 ns across all samples. The rise time is largely independent of pulse height for all but the smallest signals. For very small pulse heights (< 100 mV) rise times are significantly larger, which suggests that the deposited charge takes a longer time to be collected. This may be due to charge transport occurring via diffusion rather than drift. A gradual reduction in the rise time is observed as the total deposited charge, which is proportional to the pulse height, increases. This is expected as larger charge deposits in the sensor bulk lead to a greater rate of charge collection by the CCPDv3 and a smaller time taken for the pulse height to reach the peak. As the intrinsic performance of the CCPDv3 sensors in the devices tested is very similar, comparisons of the misaligned samples will be made more straightforward. As nearly identical intrinsic performance was observed for the CLICpix readout chips, as will be shown in section 4.3.2, any performance differences observed between these devices will be entirely due to the capacitive glue layer and the pad alignment.

4.3.1.4 Results: ToT vs Pulse Height

The mean ToT measured in the CLICpix as a function of the CCPDv3 output voltage pulse height is shown in figure 4.8. Determination of the mean and error bars for the ToT as a function of pulse height measurement is identical to that described above for the rise time as a function of pulse height measurement.

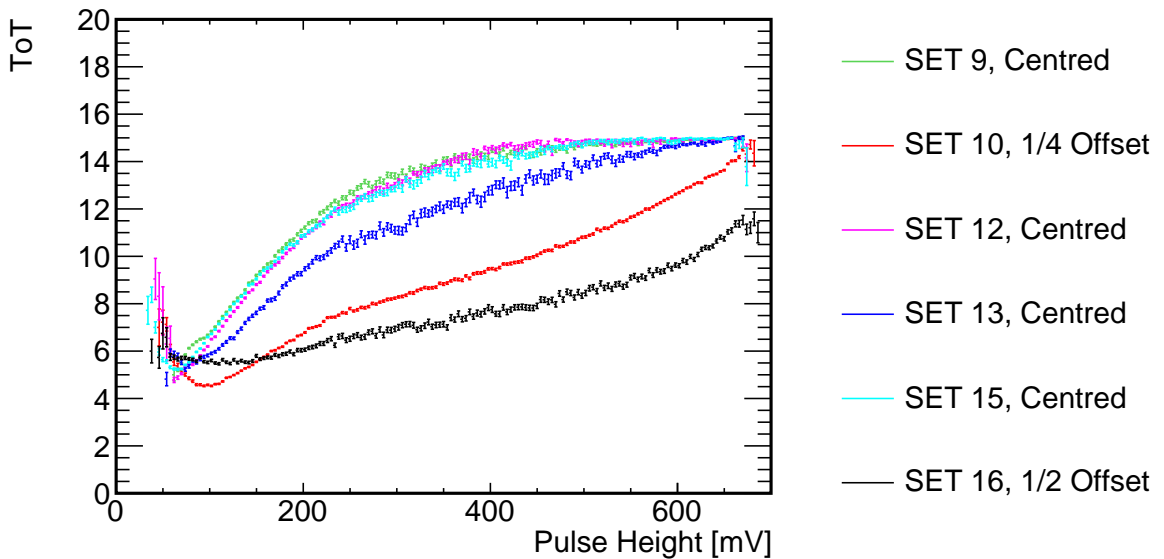


Figure 4.8: The mean ToT measured on the CLICpix ASIC as a function of CCPDv3 voltage pulse height.

For samples where the CCPDv3 and CLICpix are centred, the distribution of the mean ToT against pulse height shows that the ToT increases with pulse height up to values of approximately 400 mV and for larger pulse heights the mean ToT saturates at ≈ 15 . It is expected that the $\frac{1}{4}$ - and $\frac{1}{2}$ -offset samples will have a lower ToT than the centred samples due to the lower effective capacitance between the CCPDv3 and CLICpix pads. The greater the offset, the smaller the effective capacitance to the target CLICpix pad will be, and so the lower the recorded ToT. This is can be seen when comparing the centred samples to SET 10, the $\frac{1}{4}$ -offset sample, and SET 16, the $\frac{1}{2}$ -offset sample. In addition to the charge injected by the radioactive source there will also be background noise present from a variety of effects such as manufacturing defects in the silicon and thermal noise. This additional charge will increase the mean ToT recorded by the CLICpix and is the most likely reason as to why the mean ToT does not smoothly tend to zero as the pulse height decreases.

4.3.1.5 Results: Cross Couplings

Capacitive coupling of the sensor to the readout ASIC can also lead to unwanted signals being induced on neighbouring pixels, due to non-zero stray capacitances. Cross-coupling is the transfer of signal from a sensor pad to the readout ASIC on an adjacent pad, which will occur if there is a non-negligible capacitance between the two pads. Signals are still transferred between the aligned sensor and readout pads, however, if the cross-capacitance is large enough unwanted additional hits in the neighbouring pads will be created. This issue is particularly relevant for this study as any misalignment between the sensor and readout pads will result in an increase in the cross-capacitance along the direction of the misalignment.

Any effects of cross-coupling can be studied using the same setup as was used in section 4.3.1.4 for the ToT against pulse height analysis, but by instead considering the ToT on the adjacent CLICpix pixel along the direction of the misalignment. The mean ToT on the adjacent pixel is shown as a function of the pulse height for all devices where the CCPDv3 and CLICpix are aligned in figure 4.9a and for the misaligned samples in figure 4.9b.

The distributions of the mean ToT on the adjacent CLICpix as a function of pulse height are governed largely by cross-coupling effects. These effects will make this distribution look similar in shape to that of the mean ToT in the target CLICpix as a function of pulse height, shown in figure 4.8. However, the gradient of the adjacent ToT distribution will be shallower than the adjacent ToT distribution as the cross-capacitance is smaller than the aligned capacitance. The exception to this is the $\frac{1}{2}$ -offset sample where the cross-capacitance and aligned capacitance will be comparable. In addition to cross-coupling, this distribution will be effected by backgrounds from electrical noise and charge being deposited in the neighbouring HV-CMOS pixels.

For the centred samples, cross-coupling seems to have a small effect as the correlation between the adjacent ToT and pulse height is minimal. For the $\frac{1}{4}$ -offset sample there is a stronger correlation between the adjacent ToT and pulse height, which indicates that cross-coupling is having a more dominant effect. The gradient of the adjacent ToT vs pulse height is, however, very shallow as the cross-capacitance for this device will be relatively small. A much stronger cross-capacitive effect can be seen in the $\frac{1}{2}$ -offset sample, which is expected given it has a larger cross-capacitance than either the centred or $\frac{1}{4}$ -offset sample. The adjacent ToT distribution for the $\frac{1}{2}$ -offset sample almost mirrors the aligned ToT distribution in terms of both shape and width of the distribution. There

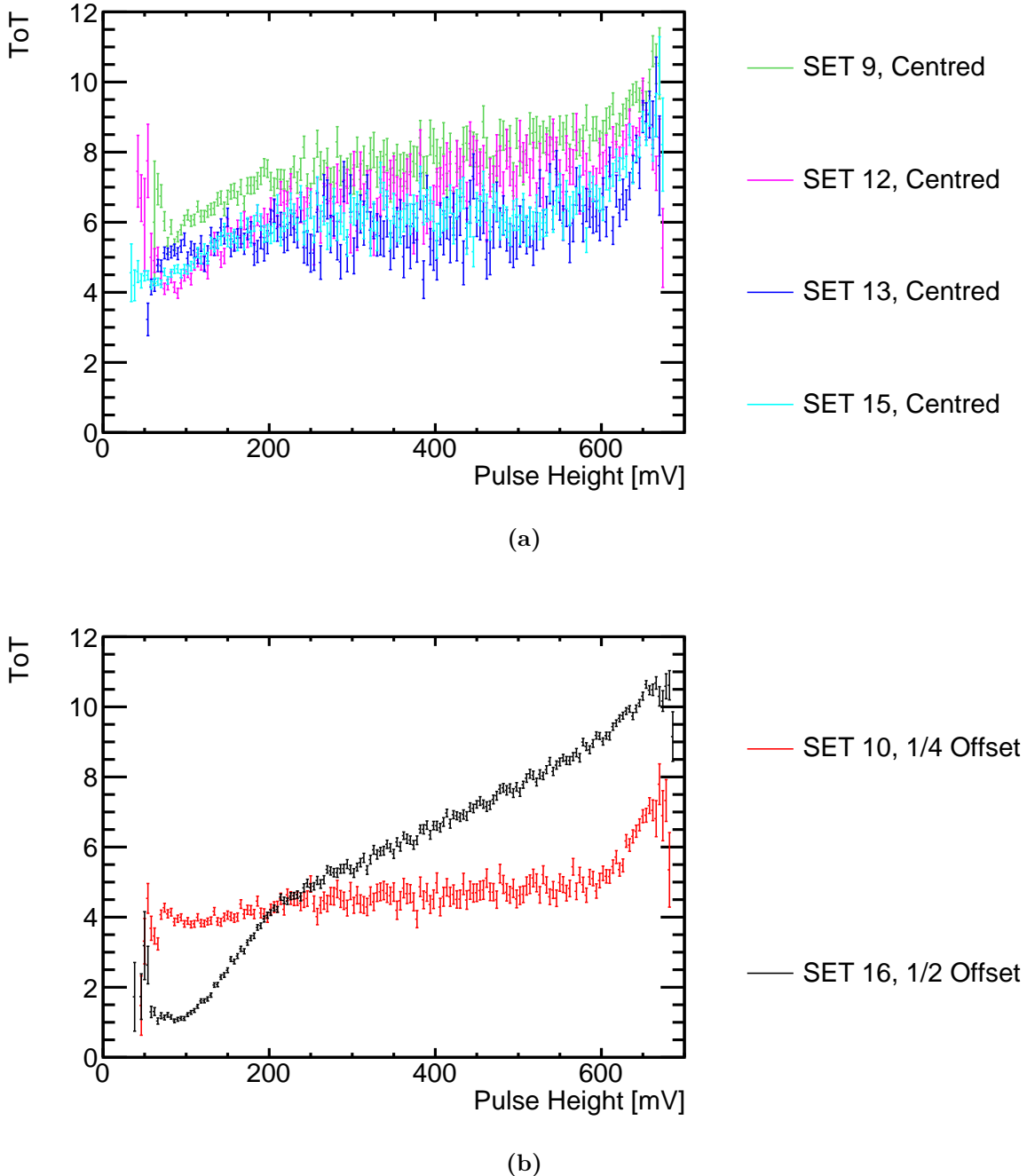


Figure 4.9: The mean ToT measured on the adjacent CLICpix pixel, along the direction of the offset, as a function of CCPDv3 voltage pulse height for (a) the centred and (b) the misaligned devices.

are some small differences between the shape of the aligned and adjacent ToT vs pulse height distribution for the $\frac{1}{2}$ -offset sample, but this is understood to be from the column structure of the CLICpix readout ASIC, more details of which can be found in section

4.3.2. Overall, these results indicate that, as expected, the misalignment of between the CCPDv3 and CLICpix pads increases the effect of cross-coupling along the direction of the misalignment.

4.3.2 Test Pulse Calibration

In order to fully understand the charge transfer to the CLICpix, a calibration of the CLICpix front-end electronics response was performed. This was achieved by directly injecting a voltage pulse of fixed height directly into a capacitor help in each CLICpix pixel. This capacitor will then inject a known amount of charge into the pixel, and by varying the height of the pulse applied the response of the CLICpix to different amounts of charge can be quantified. This experiment extends the characterisation of the CLICpix chip beyond what was found using the radioactive source measurements, as applying the voltage directly to the CLICpix fully isolates the response of the chip from any effects relating to the glue layer or CCPDv3.

4.3.2.1 Experimental Setup

To prevent any influence from neighbouring pixels during the testpulse measurements the matrix was pulsed in stages. Charge was injected into 1 out of every 16 pixels while masking the others to ensure issues related to power consumption were not encountered. This was repeated 15 more times using different mask configurations until the entire matrix had been sampled. This procedure was repeated 100 times to determine the average ToT response on a per-pixel level. The pulse height injected into the CLICpix was varied from 2 to 180 mV in steps of 2 mV in order to fully characterise the response up to saturation of the ToT output. An example of the mean ToT plotted against the injected pulse height is shown in figure 4.10.

4.3.2.2 Analysis

The functional form of the ToT against pulse height plot will be described using a surrogate function [52]

$$y = ax + b - \frac{c}{x - t}, \quad (4.1)$$

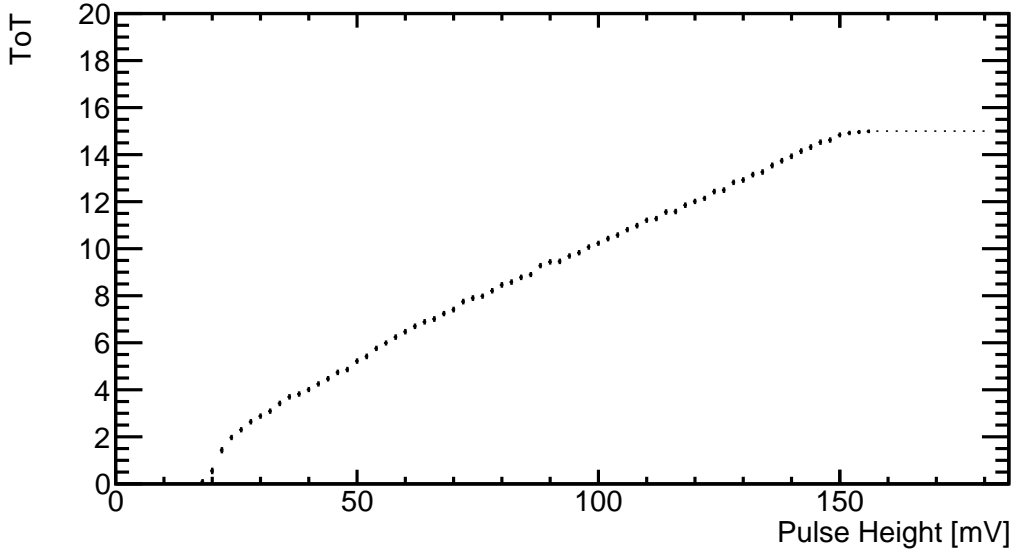


Figure 4.10: The CLICpix ToT as a function of injected pulse height. The black markers show the mean ToT and the error bars show the standard error.

where y is the ToT, x is the pulse height in mV and a , b , c and t are fit parameters. Application of the fit helps to condense the large amount of data recorded for an individual pixel down to a small number of parameters, which makes categorisation of the response of the CLICpix matrix more clear. At large pulse heights the linear relationship dominates while for low pulse heights the inversely proportional term dominates. c describes the curvature of the graph, while t determines the asymptote below which no signal is detected. Figure 4.11 shows an example of the application of this fit. As this function does not describe saturation of the ToT or the region below threshold, the fit is only applied on data points where the mean ToT is greater than 1 and less than 14.75.

4.3.2.3 Results

A known issue with the design of the CLICpix ASIC is the unwanted feedback capacitance between the discriminator output and amplifier input. This feedback leads to an additional fixed injected charge being measured for each recorded hit, due to the firing of the discriminator. The magnitude of this effect differs between even and odd columns across the CLICpix matrix due to slight differences in the physical layouts of alternating columns. By examining the distribution of the surrogate fit parameters, shown for SET 9 in figure 4.12, this effect can be seen.

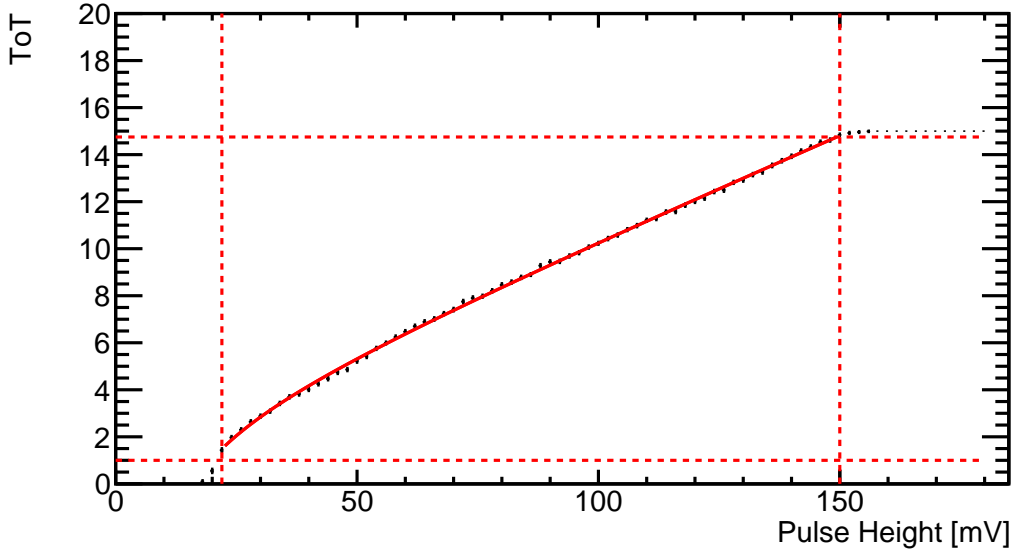


Figure 4.11: CLICpix ToT as a function of injected pulse height for a single pixel. The black markers are the mean ToT and the error bars are the standard error on the mean. The solid red line shows the surrogate function fit and the dotted red lines show the range where the fit was applied.

The peaks at zero in the distribution of the a and b parameters, containing ≈ 150 entries, correspond to noisy and dead pixels. These damaged pixels will be found in the device due to problems occurring in the manufacturing process. The majority of the a and b parameters are centred around a single value, which indicates a similar response in the linear region of the surrogate function, however, the c and t parameters are centred around one of two values. When examining the distribution of these parameters as a function of position on the matrix, shown in figure 4.13 for a selected device, it can be seen that the structure is related to the column a given pixel is in. This feature is present in all devices considered and the underlying cause, the unwanted feedback capacitance, will be remedied in the next generation of the CLICpix ASIC.

The matrix-averaged surrogate function fit parameters for all devices can be found in tables 4.2 and 4.3, for the even and odd columns respectively. The surrogate function for each device using these average parameters as input is shown in figure 4.14.

As figure 4.14 shows, the response of the CLICpix to the injected pulse height is largely uniform across all samples. For all devices the turn-on pulse height is ≈ 10 mV and saturation, which occurs when the ToT output reaches the maximum value of 15, occurs at

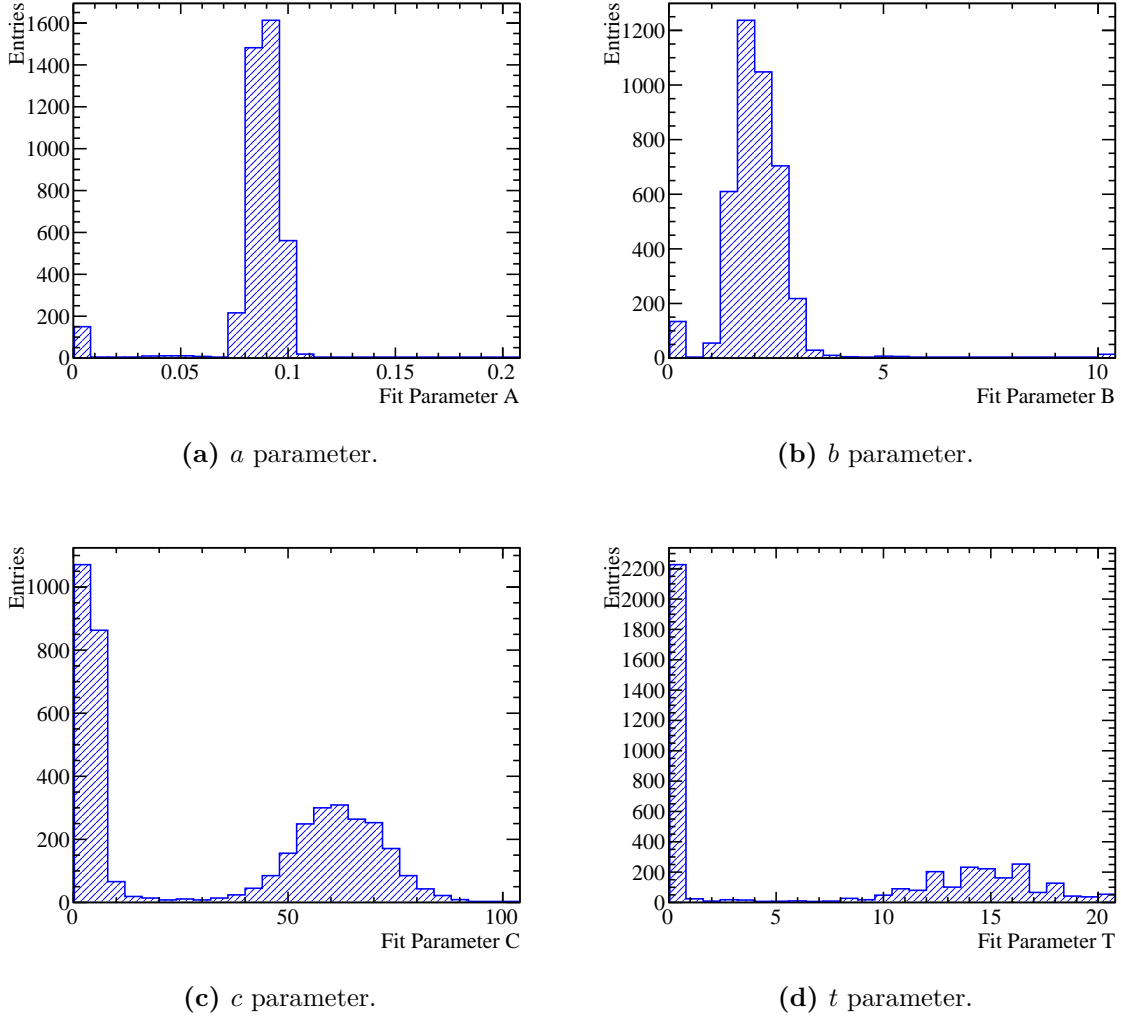


Figure 4.12: The distribution of the surrogate function parameters obtained when fitting the ToT as a function of injected pulse height for SET 9. (a), (b), (c) and (d) show the distribution of the a , b , c and d parameters respectively.

≈ 150 mV. The differing column structure exists due to the unwanted feedback capacitance between the discriminator output and amplifier input. This unwanted feedback leads to a sharper rise in ToT for even-numbered columns than for odd-numbered columns, as in effect the even-numbered columns are operating at a lower threshold. This column structure is present in all devices considered. The uniformity of the response of the CLICpix ASICs observed in this study make comparisons between the misaligned samples clearer. These results show that any performance differences observed between the misaligned devices do not originate from the intrinsic behaviour of the CLICpix ASIC.

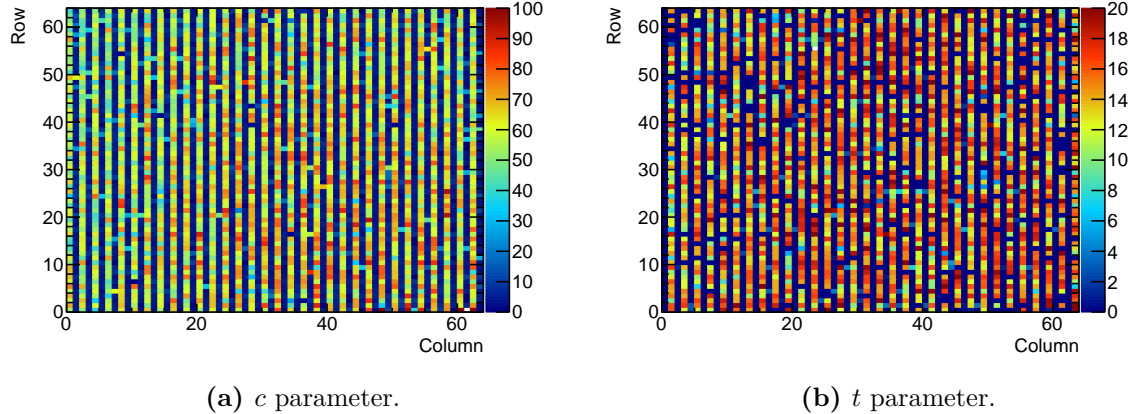


Figure 4.13: The distribution of selected surrogate function parameters obtained when fitting the ToT as a function of injected pulse height for SET 9 as a function of matrix position. (a) and (b) show the distribution of the c and t parameters respectively.

| Assembly | a | b | c | t |
|----------|---------------------|-----------------|----------------|------------------|
| SET 9 | 0.0875 ± 0.0005 | 2.41 ± 0.03 | 5.1 ± 0.1 | 12.79 ± 0.15 |
| SET 10 | 0.0769 ± 0.0005 | 2.58 ± 0.03 | 7.5 ± 0.2 | 8.02 ± 0.14 |
| SET 12 | 0.0725 ± 0.0005 | 2.87 ± 0.04 | 12.1 ± 0.3 | 7.86 ± 0.22 |
| SET 13 | 0.0708 ± 0.0005 | 2.69 ± 0.03 | 16.2 ± 0.3 | 6.65 ± 0.18 |
| SET 15 | 0.0856 ± 0.0005 | 2.34 ± 0.03 | 5.1 ± 0.2 | 12.51 ± 0.13 |
| SET 16 | 0.0746 ± 0.0004 | 2.32 ± 0.02 | 13.7 ± 0.3 | 6.65 ± 0.16 |

Table 4.2: The average fit parameters for even columns of CLICpix sensor. The reported error was calculated using the standard error in the mean when averaging the fit parameters across the matrix.

4.4 Test Beam Analysis

Test beam measurements were used to characterise the behaviour of the prototype capacitively coupled pixel detectors. These measurements are particularly useful as they include information relating to the properties of the particles passing through the device under test (DUT). This information is crucial for calculating the efficiency of the devices, which will ultimately determine whether the device is fit for use in the CLIC vertex detector.

The trajectory of any particles passing through the DUT was measured in the test beam setup using a telescope. The telescope consisted of several planes of pixel detectors

| Assembly | a | b | c | t |
|----------|---------------------|-----------------|----------------|-----------------|
| SET 9 | 0.0834 ± 0.0003 | 1.72 ± 0.01 | 61.0 ± 0.3 | 0.25 ± 0.09 |
| SET 10 | 0.0759 ± 0.0002 | 1.63 ± 0.01 | 43.2 ± 0.2 | 0.10 ± 0.02 |
| SET 12 | 0.0731 ± 0.0003 | 1.92 ± 0.02 | 51.5 ± 0.3 | 0.36 ± 0.12 |
| SET 13 | 0.0713 ± 0.0002 | 1.72 ± 0.01 | 52.5 ± 0.3 | 0.18 ± 0.07 |
| SET 15 | 0.0836 ± 0.0003 | 1.52 ± 0.02 | 52.7 ± 0.3 | 0.42 ± 0.08 |
| SET 16 | 0.0727 ± 0.0002 | 1.49 ± 0.01 | 50.7 ± 0.2 | 0.10 ± 0.03 |

Table 4.3: The average fit parameters for odd columns of CLICpix sensor. The reported error was calculated using the standard error in the mean when averaging the fit parameters across the matrix.

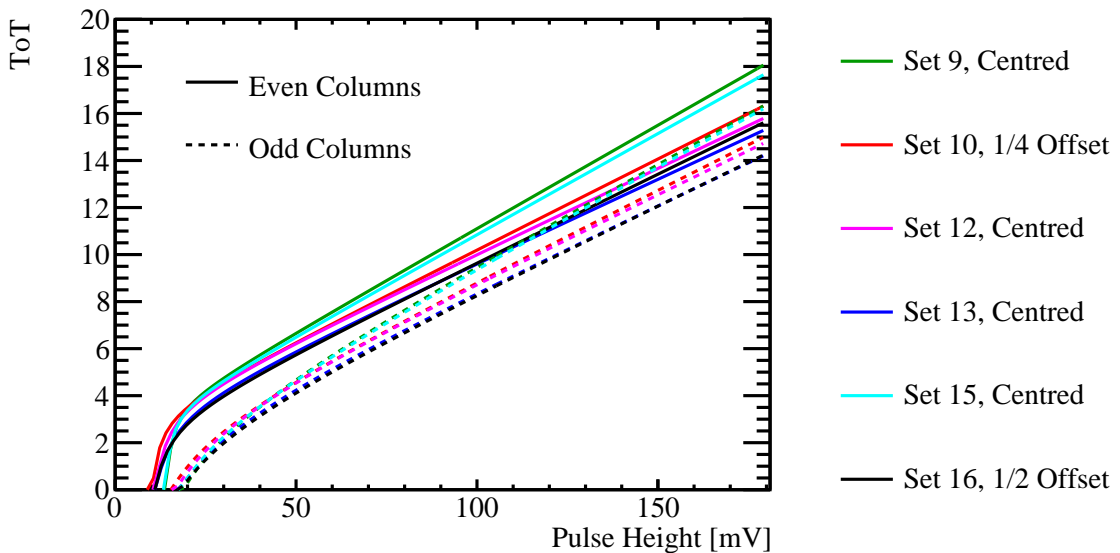


Figure 4.14: The average ToT response as a function of injected pulse height, which is represented using the surrogate function. Parameters for the surrogate function are obtained by fitting the ToT against pulse height curve for all pixels in the matrix. The results are divided into even and odd columns to account for the differing effective thresholds on alternate CLICpix columns.

mounted either side of the DUT. As low energy particles would be stopped by the telescope detector planes, telescopes can only be used to measure the trajectory of relatively high energy particles. This means that they cannot be used in lab based measurements, but can be used in test beams where high energy particles can be safely produced.

4.4.1 Test Beam Setup

Test beam experiments were carried out in August and September 2015 on the H6 beam line in the CERN SPS North Area. The beam consisted of positively charged hadrons of momenta 120 GeV/c. Mean particle rates of 500 kHz/cm^2 were observed during the 4.8 s spills at intervals of 25 s. The devices under test were mounted on an EUDET/AIDA telescope [53]. This telescope consisted of six planes of sensors, three on either side of the DUT, constructed of Mimosa pixel detectors. This telescope provided a resolution of 1.6 μm on the intercept position between tracks passing through the device and the DUT mounted on it.

4.4.2 Analysis

A number of cuts were applied to veto the effect of noisy pixels and tracks that underwent non-negligible multiple scattering. These effects would lead to discrepancies in the reported efficiencies of the devices, which are not representative of the true device performance. Any pixels identified on the DUT that were deemed to be noisy were removed from the analysis. A pixel was deemed noisy if it responded at a mean rate greater than 5σ in comparison to the average rate across the whole matrix. In addition to this, any tracks with an intercept on the DUT within half a pixel width of a noisy pixel were also rejected from the analysis. As tracks may undergo non-negligible multiple scattering, a χ^2 cut was used to remove less precisely reconstructed tracks. Furthermore, all tracks occurring within 125 μm of each other were vetoed, in order to reduce the possibility of mis-association of clusters to tracks.

After the application of these cuts, the track position on the DUT was calculated using the measured particle trajectory through the telescope planes. This was followed by a search around the intercept position on the DUT to find an associated cluster. Clusters were associated to the track if they fell within 75 μm , or 3 pixels, about the intercept position. If multiple clusters were associated to a track the cluster position was calculated as the ToT-weighted centre-of-gravity.

Alignment of the telescope planes was essential for ensuring that the correct trajectory of the particles passing through the setup could be determined. Furthermore, alignment of the DUT with respect to the telescope planes was critical for ensuring the correct track intercept position was found. With that in mind the six telescope planes were aligned by minimising the total track χ^2 with respect to the global alignment parameters. The

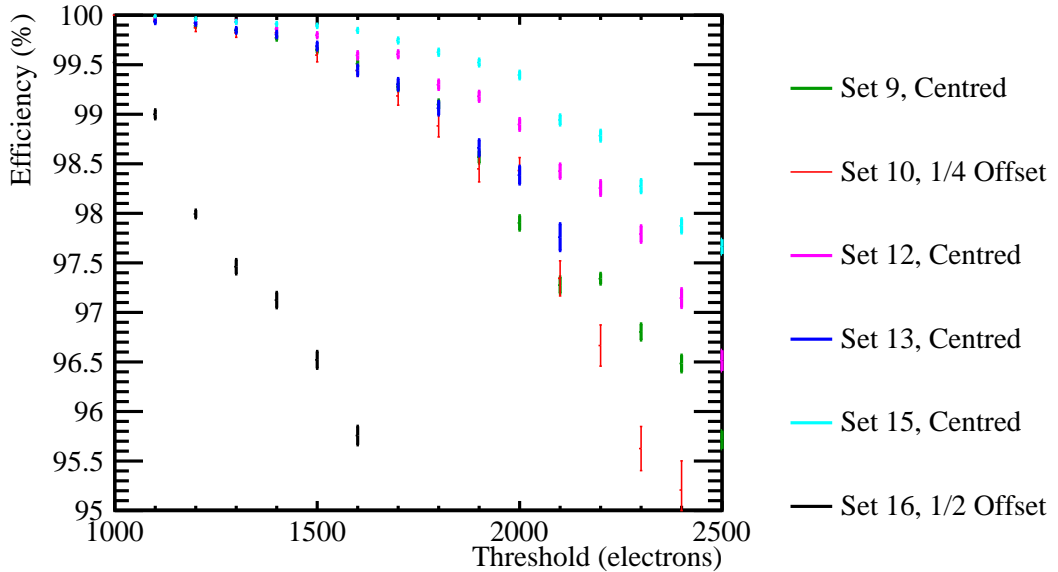


Figure 4.15: The efficiency of the devices considered as a function of the threshold applied.

tracks that were created in the alignment procedure are referred to as "rough tracks" as they are produced using the hits from sensor planes that may not be ideally aligned. The alignment proceeded one telescope plane at a time until all planes were accounted for. This procedure was iteratively repeated, updating the global alignment parameters to the optimal values found each time, until no further gains could be made. Once the telescope planes were aligned, the DUT was aligned in a similar manor, but this time minimising the summed square of track residuals. The residual is defined as the difference between the track intercept and associated cluster centre-of-gravity.

4.4.3 Results

The metric used for characterising the device performance in the test beam is the single hit efficiency, ϵ . This is defined as the number of tracks with associated clusters recorded by the DUT, n , divided by the number of reconstructed tracks passing through the DUT recorded by the telescope, m . The errors shown on the efficiency measurements are given by $\sqrt{\frac{\epsilon(1-\epsilon)}{m}}$, which follows from the variance of n given binomial statistics with mean ϵ . The single hit efficiency as a function of threshold for all devices is shown in figure 4.15. The threshold, in units of number of electrons, is the size of the signal that must be injected into the CLICpix ASIC to generate a hit.

The data indicates that for all assemblies the single hit efficiency of the detector decreases when a higher amount of charge is required to generate a signal, which is to be expected. However, the efficiency of all samples, with the exception of the $\frac{1}{2}$ -offset sample, is still above 99% up to a threshold of 2000 electrons. This is encouraging behaviour as the larger the threshold that can be applied the lower the effects from noise will be. Reducing the effects from noise will aid tracking performance in the CLIC vertex detector, which is highly desirable. It is clear that the $\frac{1}{2}$ offset sample, SET 16, has a much lower efficiency as a function of threshold in comparison to the other samples. For the same deposited charge in the CCPDv3 the $\frac{1}{2}$ -offset sample will, due to the reduced capacitance, produce a smaller signal in the CLICpix than the centred samples. This is the cause of the reduced efficiency as a function of threshold in this sample. More encouragingly is the behaviour of the $\frac{1}{4}$ -offset sample, SET 14, which in terms of performance is comparable to the aligned samples. There is a degradation in efficiency of the $\frac{1}{4}$ -offset sample with respect to the aligned sample, which is to be expected given the reduced capacitance, however, it is relatively small. These results indicate that even with a relatively large misalignment between the CCPDv3 and CLICpix pads the device performance is not significantly affected, and therefore manufacturing tolerances of $\frac{1}{4}$ of a pixel width would not be problematic if this device were used for the CLIC vertex detector.

4.5 Conclusions

In summary, for the capacitively coupled pixel detectors considered in this analysis:

- The CCPDv3 sensor ASIC properties have been characterised and were found to be comparable across all devices.
- A calibration of the CLICpix readout ASIC was performed and their behaviour was found to be comparable across all devices.
- When combining the CCPDv3 and CLICpix characterisations, it becomes clear that any performance differences between the devices are due to the capacitive coupling gluing layer as opposed to the intrinsic behaviour of the ASICs.
- Test beam analysis of the devices found that device fabrication tolerances of up to $\frac{1}{4}$ of a pixel width would not harm the performance of these devices should they be used for the CLIC vertex detector.

Colophon

This thesis was made in L^AT_EX 2 _{ε} using the “heptesis” class [54].

Bibliography

- [1] Georges Aad et al. Observation of a new particle in the search for the Standard Model Higgs boson with the ATLAS detector at the LHC. *Phys. Lett.*, B716:1–29, 2012.
- [2] Serguei Chatrchyan et al. Observation of a new boson at a mass of 125 GeV with the CMS experiment at the LHC. *Phys. Lett.*, B716:30–61, 2012.
- [3] Ties Behnke, James E. Brau, Brian Foster, Juan Fuster, Mike Harrison, James McEwan Paterson, Michael Peskin, Marcel Stanitzki, Nicholas Walker, and Hitoshi Yamamoto. The International Linear Collider Technical Design Report - Volume 1: Executive Summary. 2013.
- [4] Lucie Linssen, Akiya Miyamoto, Marcel Stanitzki, and Harry Weerts. Physics and Detectors at CLIC: CLIC Conceptual Design Report. 2012.
- [5] M Aicheler, P Burrows, M Draper, T Garvey, P Lebrun, K Peach, N Phinney, H Schmickler, D Schulte, and N Toge. A Multi-TeV Linear Collider Based on CLIC Technology. 2012.
- [6] B. Pilicer, Helmut Burkhardt, Laurent Gatignon, Andrea Latina, Ercan Pilicer, Daniel Schulte, İlhan Tapan, and Rogelio Tomás. Study of Muon Backgrounds in the CLIC Beam Delivery System. page TUPTY032, 2015.
- [7] André Sailer. *Radiation and Background Levels in a CLIC Detector due to Beam-Beam Effects*. PhD thesis, CERN, 2012-05-09.
- [8] David J. Griffiths. *INTRODUCTION TO ELEMENTARY PARTICLES*. 1987.
- [9] Michael E. Peskin and Daniel V. Schroeder. *An Introduction to quantum field theory*. 1995.
- [10] J. Beringer et al. Review of Particle Physics (RPP). *Phys. Rev.*, D86:010001, 2012.

-
- [11] Steven Weinberg. A Model of Leptons. *Phys. Rev. Lett.*, 19:1264–1266, 1967.
 - [12] Jeffrey Goldstone, Abdus Salam, and Steven Weinberg. Broken Symmetries. *Phys. Rev.*, 127:965–970, 1962.
 - [13] John Ellis. Higgs Physics. In *Proceedings, 2013 European School of High-Energy Physics (ESHEP 2013): Paradfurdo, Hungary, June 5-18, 2013*, pages 117–168, 2015.
 - [14] K. A. Olive et al. Review of Particle Physics. *Chin. Phys.*, C38:090001, 2014.
 - [15] R. Keith Ellis, W. James Stirling, and B. R. Webber. QCD and collider physics. *Camb. Monogr. Part. Phys. Nucl. Phys. Cosmol.*, 8:1–435, 1996.
 - [16] J. R. Andersen et al. Discovering Technicolor. *Eur. Phys. J. Plus*, 126:81, 2011.
 - [17] Christophe Grojean. New approaches to electroweak symmetry breaking. *Phys. Usp.*, 50:1–35, 2007. [Usp. Fiz. Nauk177,3(2007)].
 - [18] Celine Degrande, Oscar Eboli, Bastian Feigl, Barbara Jäger, Wolfgang Kilian, Olivier Mattelaer, Michael Rauch, Jürgen Reuter, Marco Sekulla, and Doreen Wackerlo. Monte Carlo tools for studies of non-standard electroweak gauge boson interactions in multi-boson processes: A Snowmass White Paper. In *Proceedings, 2013 Community Summer Study on the Future of U.S. Particle Physics: Snowmass on the Mississippi (CSS2013): Minneapolis, MN, USA, July 29-August 6, 2013*, 2013.
 - [19] Christopher Arzt. Reduced effective Lagrangians. *Phys. Lett.*, B342:189–195, 1995.
 - [20] Ben Gripaios. Lectures on Effective Field Theory. 2015.
 - [21] Maria J. Herrero and Ester Ruiz Morales. The Electroweak chiral Lagrangian as an effective field theory of the standard model with a heavy Higgs. In *Workshop on Electroweak Symmetry Breaking Budapest, Hungary, July 11-13, 1994*, pages 37–54, 1994.
 - [22] Anthony C. Longhitano. Low-Energy Impact of a Heavy Higgs Boson Sector. *Nucl. Phys.*, B188:118–154, 1981.
 - [23] A. S. Belyaev, Oscar J. P. Eboli, M. C. Gonzalez-Garcia, J. K. Mizukoshi, S. F. Novaes, and I. Zacharov. Strongly interacting vector bosons at the CERN LHC: Quartic anomalous couplings. *Phys. Rev.*, D59:015022, 1999.
 - [24] M. A. Thomson. Particle Flow Calorimetry and the PandoraPFA Algorithm. *Nucl.*

- Instrum. Meth.*, A611:25–40, 2009.
- [25] J. S. Marshall, A. Münnich, and M. A. Thomson. Performance of Particle Flow Calorimetry at CLIC. *Nucl. Instrum. Meth.*, A700:153–162, 2013.
 - [26] Halina Abramowicz et al. The International Linear Collider Technical Design Report - Volume 4: Detectors. 2013.
 - [27] Toshinori Abe et al. The International Large Detector: Letter of Intent. 2010.
 - [28] Toshinori Abe et al. The International Large Detector: Letter of Intent. 2010.
 - [29] Serguei Chatrchyan et al. Energy Calibration and Resolution of the CMS Electromagnetic Calorimeter in pp Collisions at $\sqrt{s} = 7$ TeV. *JINST*, 8:P09009, 2013. [JINST8,9009(2013)].
 - [30] M. Aharrouche et al. Energy linearity and resolution of the ATLAS electromagnetic barrel calorimeter in an electron test-beam. *Nucl. Instrum. Meth.*, A568:601–623, 2006.
 - [31] Pascal Perret. First Years of Running for the LHCb Calorimeter System. *PoS*, TIPP2014:030, 2014.
 - [32] Huong Lan Tran, Katja Krüger, Felix Sefkow, Steven Green, John Marshall, Mark Thomson, and Frank Simon. Software compensation in Particle Flow reconstruction. 2017.
 - [33] M. Chefdeville et al. Shower development of particles with momenta from 15 GeV to 150 GeV in the CALICE scintillator-tungsten hadronic calorimeter. *JINST*, 10(12):P12006, 2015.
 - [34] Howard S. Budd. CMS central hadron calorimeter. *Nucl. Phys. Proc. Suppl.*, 54B:191–197, 1997. [,191(2001)].
 - [35] A. Airapetian et al. ATLAS calorimeter performance Technical Design Report. 1996.
 - [36] P. Mora de Freitas and H. Videau. Detector simulation with MOKKA / GEANT4: Present and future. In *Linear colliders. Proceedings, International Workshop on physics and experiments with future electron-positron linear colliders, LCWS 2002, Seogwipo, Jeju Island, Korea, August 26-30, 2002*, pages 623–627, 2002.
 - [37] S. Agostinelli et al. GEANT4: A Simulation toolkit. *Nucl. Instrum. Meth.*, A506:250–303, 2003.

- [38] J. B. Birks. Scintillations from Organic Crystals: Specific Fluorescence and Relative Response to Different Radiations. *Proc. Phys. Soc.*, A64:874–877, 1951.
- [39] F. Gaede. Marlin and LCCD: Software tools for the ILC. *Nucl. Instrum. Meth.*, A559:177–180, 2006.
- [40] H. Abramowicz et al. Higgs Physics at the CLIC Electron-Positron Linear Collider. 2016.
- [41] Torbjorn Sjostrand, Stephen Mrenna, and Peter Z. Skands. PYTHIA 6.4 Physics and Manual. *JHEP*, 05:026, 2006.
- [42] G. Alexander et al. A Comparison of b and u d s quark jets to gluon jets. *Z. Phys.*, C69:543–560, 1996.
- [43] Z. Was. TAUOLA the library for tau lepton decay, and KKMC / KORALB / KORALZ /... status report. *Nucl. Phys. Proc. Suppl.*, 98:96–102, 2001. [,96(2000)].
- [44] Serguei Chatrchyan et al. Measurement of the $W\gamma$ and $Z\gamma$ inclusive cross sections in pp collisions at $\sqrt{s} = 7\text{TeV}$ and limits on anomalous triple gauge boson couplings. *Phys. Rev.*, D89(9):092005, 2014.
- [45] Georges Aad et al. Measurement of W^+W^- production in pp collisions at $\sqrt{s} = 7\text{TeV}$ with the ATLAS detector and limits on anomalous WWZ and WW $\tilde{t}\tilde{t}$ couplings. *Phys. Rev.*, D87(11):112001, 2013. [Erratum: Phys. Rev.D88,no.7,079906(2013)].
- [46] Serguei Chatrchyan et al. Search for $WW\gamma$ and $WZ\gamma$ production and constraints on anomalous quartic gauge couplings in pp collisions at $\sqrt{s} = 8\text{TeV}$. *Phys. Rev.*, D90(3):032008, 2014.
- [47] C. W. Fabjan and F. Gianotti. Calorimetry for particle physics. *Rev. Mod. Phys.*, 75:1243–1286, 2003.
- [48] C. Adloff et al. Hadronic energy resolution of a highly granular scintillator-steel hadron calorimeter using software compensation techniques. *JINST*, 7:P09017, 2012.
- [49] M. Benoit et al. Testbeam results of irradiated ams H18 HV-CMOS pixel sensor prototypes. 2016.
- [50] Roel Aaij, Adeva, et al. Expression of Interest for a Phase-II LHCb Upgrade: Opportunities in flavour physics, and beyond, in the HL-LHC era. Technical Report CERN-LHCC-2017-003, CERN, Geneva, Feb 2017.

- [51] A Dominguez, D Abbaneo, K Arndt, N Bacchetta, A Ball, E Bartz, W Bertl, G M Bilei, G Bolla, H W K Cheung, M Chertok, S Costa, N Demaria, Daniel Dominguez Vazquez, K Ecklund, W Erdmann, K Gill, G Hall, K Harder, F Hartmann, R Horisberger, W Johns, H C Kaestli, K Klein, D Kotlinski, S Kwan, M Pesaresi, H Postema, T Rohe, C Schafer, A Starodumov, S Streuli, A Tricomi, P Tropea, J Troska, F Vasey, and W Zeuner. CMS Technical Design Report for the Pixel Detector Upgrade. Technical Report CERN-LHCC-2012-016. CMS-TDR-11, Sep 2012. Additional contacts: Jeffrey Spalding, Fermilab, Jeffrey.Spalding@cern.ch Didier Contardo, Universite Claude Bernard-Lyon I, didier.claude.contardo@cern.ch.
- [52] Niloufar Alipour Tehrani, Samir Arfaoui, Mathieu Benoit, Damiano Celeste, Dominik Dannheim, Florentina Pfleger, and Sophie Redford. Calibration of ultra-thin hybrid pixel detector assemblies with Timepix readout ASICs. Sep 2015.
- [53] I Rubinskiy. An EUDET/AIDA Pixel Beam Telescope for Detector Development. (AIDA-CONF-2015-035), Jun 2011.
- [54] Andy Buckley. The *heptesis* L^AT_EX class.